Supplementary Information for

Hydroxyl chemistry regulation of cellulose biopolymers for aqueous zinc battery binders

Rongfu Xu (许荣富)[1,2,3,‡], Ningxin Chen (陈宁昕)[3,‡], Zichan Yuan (袁紫婵)[3], Zihan Guo (郭子瀚)[3], Jie Deng (邓婕)[3], En Chen (陈恩)[3], Yinglin Yan (燕映霖)[1*], Xianhui Wang (王献辉)[2], Chaoji Chen (陈朝吉)[4,5*], Zhaohui Wang (汪朝晖)[3*]

[1]State Key Laboratory of Water Engineering Ecology and Environment in Arid Area, School of Eco-environmental and Chemical Engineering, Xi'an University of Technology, Xi'an, 710048, P. R. China.

[2]School of Materials Science and Engineering, Xi'an University of Technology, Xi'an, 710048, P. R. China.

[3]Department of Materials Science and Engineering, Hunan University, Changsha, 410082, P. R. China.

[4]Hubei Biomass-Resource Chemistry and Environmental Biotechnology Key Laboratory, School of Resource and Environmental Sciences, Wuhan University, Wuhan 430079, P. R. China.

[5]Hubei Provincial Engineering Research Center of Emerging Functional Coating Materials, School of Resource and Environmental Sciences, Wuhan University, Wuhan 430079, P. R. China.

[‡]These authors contribute equally.

[*]Corresponding authors: yyl3550@xaut.edu.cn (Y. Yan); chenchaojili@whu.edu.cn (C. Chen); sunnywang@hnu.edu.cn (Z. Wang)

Table of Contents

Supplementary Fig. 6. The schematic illustrations of interchain hydrogen bond distributions in **a,** CNF and **b,** ONF (as derived from the isosurface analysis in Fig. 2e).

Supplementary Fig. 7. a, CNF and **b,** ONF cellulose conformations with corresponding **c,** structural parameters. Gray, white, and blue atoms denote C, H, and O, respectively.

Supplementary Fig. 8. Transmittance spectra of CNF dispersion and ONF dispersion (1.5 mg mL^{-1}, dispersant: deionized water) in the visible wavelength range (400~760 nm).

Supplementary Fig. 9. Optical photographs of CNF dispersion and ONF dispersion after three months of static storage at room temperature.

Supplementary Fig. 10. Optical photos of the contact angle test of CNF dispersion and ONF dispersion.

Supplementary Fig. 11. Microstructure of **a,** CNF and **b,** ONF cellulose papers.

Supplementary Fig. 12. Thickness and mass comparison of **a, a1, a2,** CNF and **b, b1, b2,** ONF cellulose papers at equal surface area.

Supplementary Fig. 13. The stress-strain curves of **a,** CNF and **b,** ONF cellulose papers.

Supplementary Fig. 14. The surface fiber distribution morphology of **a,** CNF- and **b,** ONF-based positive electrodes.

Supplementary Fig. 15. Surface microstructures of PVDF-based positive electrode at different magnifications.

Supplementary Fig. 16. a-d, Surface morphology of the CNF positive electrode at different magnifications. **e-h,** Surface morphology of the ONF positive electrode at different magnifications.

Supplementary Fig. 17. Schematic illustrations of AC@I_2 particle in different iodine positive electrodes: **a,** PVDF, **b,** CNF, and **c,** ONF.

Supplementary Fig. 18. Characterization of porous structures in iodine hosts (without iodine) fabricated using different binders. **a,** Nitrogen adsorption-desorption isotherms. **b,** Specific surface area. **c,** Pore size distribution curves.

Supplementary Fig. 19. The stress-strain curves of **a,** CNF- and **b,** ONF-based positive electrodes.

Supplementary Fig. 20. Wet-state mechanical properties of CNF and ONF positive electrodes. **a,** Stress-strain curves of positive electrodes immersed in deionized water. **b,** Stress-strain curves of positive electrodes immersed in 2 M $ZnSO_4$ solution. **c,** Tensile strength and elongation of positive

electrodes after immersion in different liquids.

Supplementary Fig. 21. Thickness variation and swelling ratio of CNF and ONF positive electrodes before and after electrolyte immersion.

Supplementary Fig. 22. Electrolyte (2 M $ZnSO_4$) wettability of PVDF-, CNF-, and ONF-based positive electrodes.

Supplementary Fig. 23. CV profiles of **a,** PVDF-, **b,** CNF-, and **c,** ONF-based positive electrodes at various scan rates. All batteries were tested at 25±1.5 °C.

Supplementary Fig. 24. The oxidation peak potential and reduction peak potential as functions of sweep speed for positive electrodes using different binders. **a,** PVDF, **b,** CNF, and **c,** ONF.

Supplementary Fig. 25. a, CV profiles of PVDF-, CNF-, and ONF-based positive electrodes at 1.0 mV s^{-1}, and comparative analysis of fitted slopes for **b,** oxidation and **c,** reduction peaks. All batteries were tested at 25±1.5 °C.

Supplementary Fig. 26. a, GITT profiles of PVDF-, CNF-, and ONF-based positive electrodes. **b,** Transient voltage-time curve during a typical current pulse. **c,** Verification of the linear relationship between cell voltage and the square root of time. All batteries were tested at 25±1.5 °C.

Supplementary Fig. 27. Rate capability of iodine positive electrodes with different binders. **a,** Coulombic efficiency during rate capability tests (with specific currents applied sequentially every 10 cycles: 0.2, 1, 2, 5, 10, 20, 10, 5, 2, 1, 0.2 A g^{-1}). Galvanostatic charge/discharge profiles of **b,** PVDF-, **c,** CNF-, and **d,** ONF-based positive electrodes at varying specific currents (from right to left: 0.2, 1, 2, 5, 10, and 20 A g^{-1}). All batteries were tested at 25±1.5 °C.

Supplementary Fig. 28. The rest time-voltage curves of Zn||I_2 batteries with different positive electrode binder systems. Rest durations: **a,** 24 h. **b,** 48 h. **c,** 96 h. All batteries were tested at 25±1.5 °C.

Supplementary Fig. 29. Cycling performance of iodine positive electrodes with different binders. **a,** Coulombic efficiency during cycling performance tests (with a specific current of 10 A g^{-1}). Galvanostatic charge-discharge curves of failed **b,** PVDF-based and **c,** CNF-based positive electrodes. **d,** Galvanostatic charge-discharge curves of the ONF-based positive electrode at different cycle numbers. All batteries were tested at 25±1.5 °C.

Supplementary Fig. 30. Differential capacity curves (top) of the PVDF-based positive electrode

and chronoamperometric profiles (bottom) of different positive electrodes at 1.37 V (vs. Zn^{2+}/Zn). All batteries were tested at 25±1.5 °C.

Supplementary Fig. 31. a, Long-term cycling performance of iodine positive electrodes with different binders at 0.2 A g^{-1}. **b,** Coulombic efficiency during cycling performance tests. Galvanostatic charge-discharge curves of failed **c,** PVDF-based and **d,** CNF-based positive electrodes. **e,** Galvanostatic charge-discharge curves of the ONF-based positive electrode at different cycle numbers. All batteries were tested at 25±1.5 °C.

Supplementary Fig. 32. Origin of the color shading in Fig. 4 (hollow circles represent rate performance, solid circles represent cycling performance; the size of the solid circles indicates the number of cycles, and the color represents the remaining specific capacity; see Fig. 4j for details). **a,** Summary of performance comparison among different modification strategies (**b-f**). **b,** Binder. **c,** Iodine host. **d,** Separator. **e,** Electrolyte. **f,** Zinc negative electrode. The source of the literature data shown in this figure can be found in Supplementary Table 4.

Supplementary Fig. 33. a, UV-Vis spectra of the blank sample before and after heat treatment at 60 ℃ for 2 h (inset: optical images before and after heating). **b,** UV-Vis absorption spectra of CNF/I_3^- and ONF/I_3^- dispersions after thermal treatment at 60 °C for 2 h (inset: optical images before and after heating). **c,** UV-Vis absorption spectra of CNF and ONF dispersions after thermal treatment at 60 °C for 2 h (inset: optical images before and after heating). **d,** The absorbance of different samples in **Fig. 5a**.

Supplementary Fig. 34. I 3*d* XPS spectra of CNF and ONF cellulose papers after polyiodide adsorption.

Supplementary Fig. 35. In-situ UV-Vis spectra during charge/discharge processes: **a,** PVDF-, **b,** CNF-, and **c,** ONF-based positive electrodes. The test was conducted at a specific current of 0.1 A g^{-1} and a temperature of 25±1.5 °C.

Supplementary Fig. 36. a-c, In-situ EIS and corresponding **d-f,** DRT analysis for **a, d,** PVDF-, **b, e,** CNF-, and **c, f,** ONF-based positive electrodes. The test was conducted at a specific current of 0.2 A g^{-1} and a temperature of 25±1.5 °C.

Supplementary Fig. 37. Deconvolution analysis of the DRT for PVDF-based positive electrode at 1.5 V (*vs.* Zn^{2+}/Zn).

Supplementary Fig. 38. Optical photographs of iodine positive electrodes disassembled after battery cycling. **a,** PVDF-based. **b,** CNF-based. **c,** ONF-based. The battery testing conditions: 10 A g^{-1}, 1000 cycles, 100% SoC (end of test), 25±1.5 °C.

Supplementary Fig. 39. Morphological characterization of the separator-facing surface of cycled PVDF-based positive electrode. Magnifications: **a,** ×200; **b,** ×500; **c,** ×2000. The battery testing conditions: 10 A g^{-1}, 1000 cycles, 100% SoC (end of test), 25±1.5 °C.

Supplementary Fig. 40. Characterization of Cycling Stability for CNF and ONF. **a, b,** XRD patterns. **c, d,** ATR-FTIR spectra. The battery testing conditions: 10 A g^{-1}, 50 cycles, 100% SoC (end of test), 25±1.5 °C.

Supplementary Fig. 41. Surface microstructures of cycled zinc negative electrodes on the separator side (insets: optical photographs of zinc negative electrodes): **a,** PVDF, **b,** CNF and **c,** ONF. The battery testing conditions: 10 A g^{-1}, 1000 cycles, 100% SoC (end of test), 25±1.5 °C.

Supplementary Fig. 42. Schematic illustrations of PVDF-based and ONF-based cells.

Supplementary Fig. 43. XRD patterns of cycled zinc metal negative electrodes. Testing conditions: 10 A g^{-1}, 1000 cycles, 100% SoC (end of test), 25±1.5 °C.

Supplementary Fig. 44. Cycling performance of the pouch cells at 0.2 A g^{-1}. **a,** Coulombic efficiency during cycling performance tests. **b,** Galvanostatic charge/discharge curves. The battery was tested at 25±1.5 °C.

Supplementary Fig. 45. Time-voltage profiles of the pouch cell at 0.2 A g^{-1}. The battery was tested at 25±1.5 °C.

Supplementary Fig. 46. a, The thickness of a single ONF-based positive electrode sheet (left, with an I_2 loading of ~4.0 mg cm^{-2}) and the stacked thickness of four ONF-based positive electrode sheets (right, with an I_2 loading of ~16.0 mg cm^{-2}). **b,** Coulombic efficiency during cycling performance tests of stacked four-layer ONF cathodes at 1 A g^{-1}. The battery was tested at 25±1.5 °C.

Supplementary Fig. 47. Optical photograph (left) and thickness (right) of ONF-based high-loading iodine positive electrodes prepared by the one-step method.

Supplementary Fig. 48. Structural and electrochemical performance of pouch cells with ONF-based high-loading iodine positive electrodes. **a,** Structural schematic (left) and optical photograph (right). **b,** Cycling performance at 0.1 A g^{-1}. **c,** Coulombic efficiency during cycling performance

tests. The battery was tested at 25±1.5 °C.

Supplementary Fig. 49. Surface microstructure of V_2O_5 positive electrodes fabricated with different binders: **a,** PVDF, **b,** CNF, and **c,** ONF.

Supplementary Fig. 50. High-resolution XPS spectra of the V_2O_5 positive electrodes: **a,** V 2*p* and **b,** N 1*s*.

Supplementary Fig. 51. Surface morphologies of cycled V_2O_5 positive electrodes prepared with different binders (separator side, after 5 activation cycles at 0.5 A g^{-1} followed by 50 cycles at 2 A g^{-1}): **a,** PVDF, **b,** CNF, and **c,** ONF.

Supplementary Fig. 52. Rate capability of V_2O_5 positive electrodes with different binders. Galvanostatic charge/discharge profiles at various specific currents (from right to left: 0.5, 1, 2, and 5 A g^{-1}): **a,** PVDF, **b,** CNF, and **c,** ONF. **d,** Coulombic efficiency during rate capability tests (with specific currents applied sequentially every 10 cycles: 0.5, 1, 2, 5 A g^{-1}). All batteries were tested at 25±1.5 °C.

Supplementary Fig. 53. Cycling performance of V_2O_5 positive electrodes with different binders. Galvanostatic charge/discharge profiles (After 5 activation cycles at 0.5 A g^{-1}, cycling was performed at 2 A g^{-1}): **a,** PVDF, **b,** CNF, and **c,** ONF. **d,** Coulombic efficiency during cycling performance tests. All batteries were tested at 25±1.5 °C.

Supplementary Fig. 54. a, Time-voltage curve of Zn||V_2O_5 cell during the 24h resting test. **b,** Time-voltage curve of Zn||V_2O_5 cell during the 48h resting test. **c,** Corresponding capacity retention. All batteries were tested at 25±1.5 °C.

Supplementary Fig. 55. Characterization of cycled zinc metal negative electrodes (separator side, after 5 activation cycles at 0.5 A g^{-1} followed by 50 cycles at 2 A g^{-1}) paired with V_2O_5 positive electrodes prepared with different binders (**Supplementary Fig. 51**): **a-c,** surface morphology, **d-f,** vanadium elemental mapping image, and **g-i,** map sum spectrum for **a, d, g,** PVDF, **b, e, h,** CNF, and **c, f, i,** ONF binder systems. The battery testing conditions: 100% SoC (end of test), 25±1.5 °C.

Supplementary Fig. 56. a, d, Surface morphologies and corresponding **b-c, e-f,** elemental distribution images of $LiMn_2O_4$ positive electrodes fabricated with different binders: **a-c,** PVDF, **d-f,** ONF.

Supplementary Fig. 57. Electrochemical performance of $LiMn_2O_4$ positive electrodes fabricated

with different binders. **a,** Rate capability, corresponding **b, c,** galvanostatic charge/discharge profiles, and **d,** Coulombic efficiency during rate capability tests. **e,** Cycling performance, corresponding **f, g,** galvanostatic charge/discharge profiles, and **h,** Coulombic efficiency during cycling performance tests. All batteries were tested at 25±1.5 °C.

Supplementary Fig. 58. Iodine element detection in fresh cellulose membranes. **a,** EDS spectra of CNF membrane, ONF membrane, and AC@I_2. **b,** XPS I 3*d* spectra of CNF membrane and ONF membrane.

Supplementary Tables

Supplementary Table 1. Synthesis parameters, key properties (yield, extracyclic hydroxyl content), and positive electrode performance (discharge capacity at 20 A g^{-1}) for ONFs prepared from CNF under varying conditions.

Supplementary Table 2. Four-probe measurement data for CNF-based and ONF-based electrodes.

Supplementary Table 3. Range of R_{int}-values and *D*-values during charge/discharge processes in zinc-iodine batteries with different binder systems.

Supplementary Table 4. Comparative of electrochemical performance in aqueous Zn||I_2 battery.

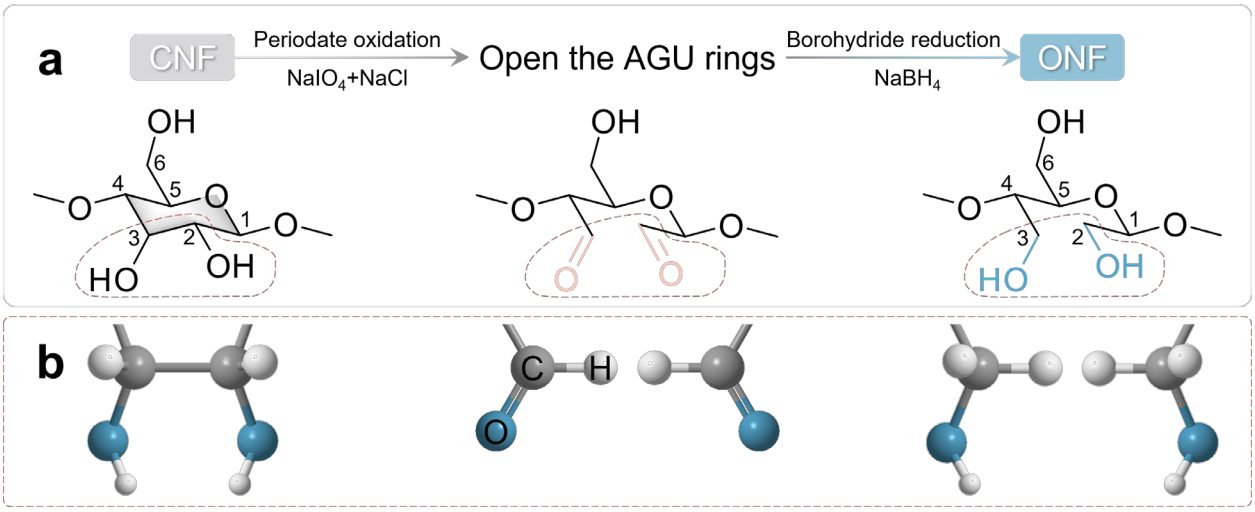

Supplementary Fig. 1. Schematic illustration of **a,** cellulose molecular structure evolution and **b,** bond transformation during the periodate-borohydride treatment.

Supplementary Note 1

As the $NaIO_4$/AGU molar ratio increases, the content of extracyclic hydroxyl (reflecting the degree of ring opening) rises gradually (**Supplementary Fig. 2**d, from 1.7 mmol g^{-1} at a ratio of 0.25 to 6.7 mmol g^{-1} at a ratio of 4). Concurrently, the yields from periodate oxidation, borohydride reduction, and the overall yield all exhibit a decreasing trend (**Supplementary Fig. 2**a-c; the total yield declines from 81.44% at a ratio of 0.25 to 0.26% at a ratio of 4).

The specific capacity of the iodine positive electrode increases with the initial rise in ring opening (**Supplementary Fig. 2**e, f). For instance, at a molar ratio of 1, the extracyclic hydroxyl content reaches 4 mmol g^{-1}, and the specific capacity rises to 150.01 mAh g^{-1} (an increase of approximately 18.3% compared with the unmodified sample), while the total yield remains relatively high at 62.81%. When the molar ratio is further increased to 2, the degree of ring opening continues to rise, but the total yield drops sharply to 42.14%, and the gain in specific capacity is only about 3.5%.

In summary, while increasing the ring-opening degree of cellulose can improve electrochemical performance, an excessively high degree of ring opening results in a dramatic reduction in yield. Therefore, a $NaIO_4$/AGU molar ratio of 1:1 was selected, as it achieves an optimal balance among ring-opening degree, yield, and electrochemical performance.

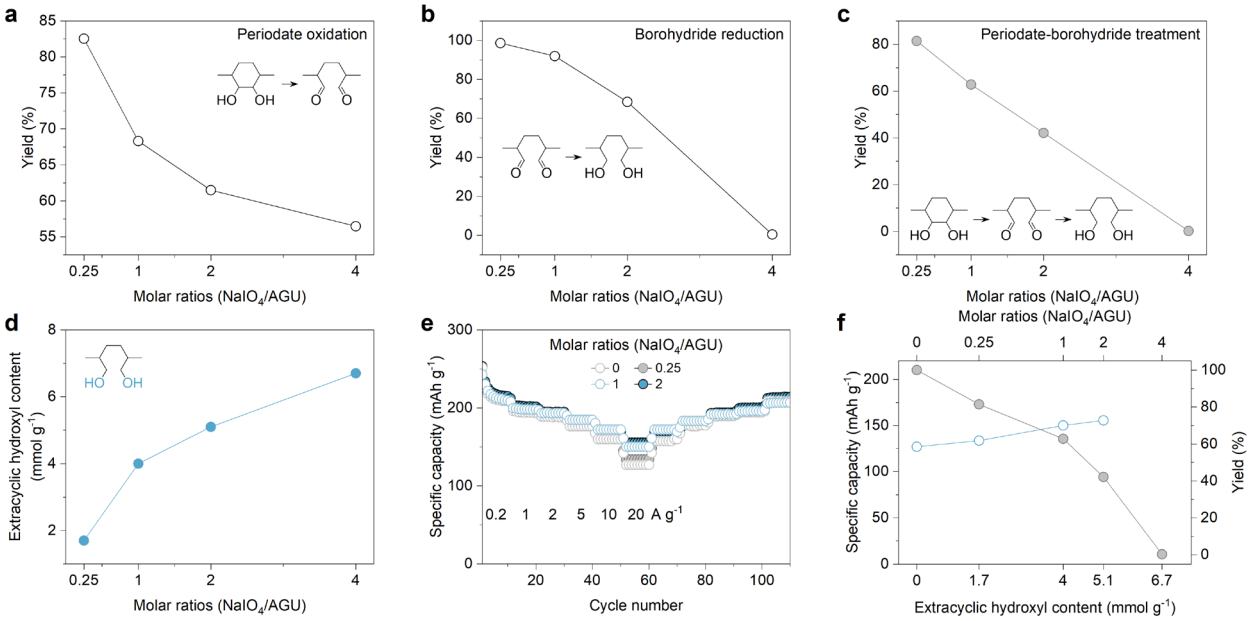

Supplementary Fig. 2. Synthesis parameters, properties, and corresponding positive electrode performance for ONF. **a-c,** Reaction yields at different $NaIO_4$/AGU molar ratios: **a,** periodate oxidation; **b,** borohydride reduction; **c,** total yield. **d,** Quantified content of extracyclic hydroxyl groups versus $NaIO_4$/AGU ratios. **e,** Rate performance of iodine positive electrodes prepared from ONFs with varying degrees of ring opening. **f,** Correlation between the degree of ring opening (extracyclic hydroxyl content) and the resulting specific capacity and total synthesis yield.

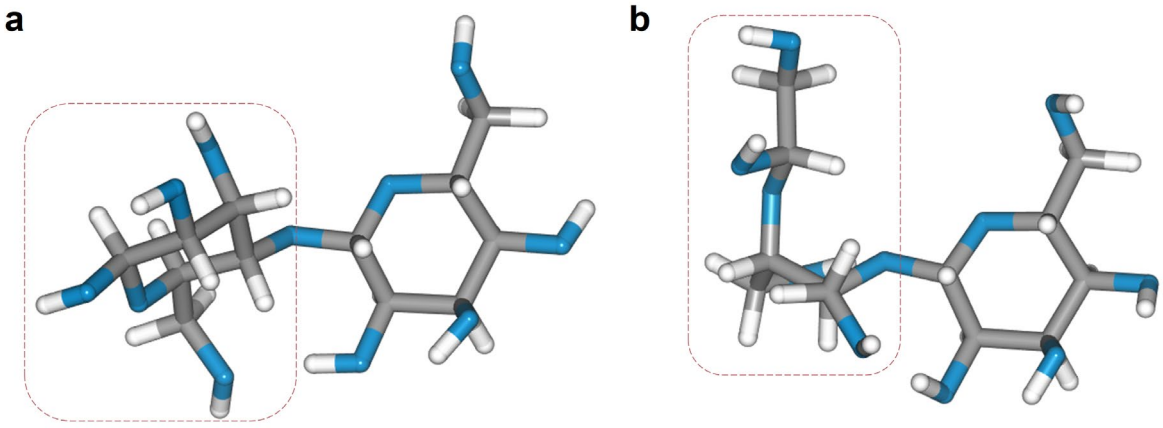

Supplementary Fig. 3. DFT-optimized molecular structures of **a,** CNF and **b,** ONF. Gray, white, and blue sticks represent C, H, and O, respectively.

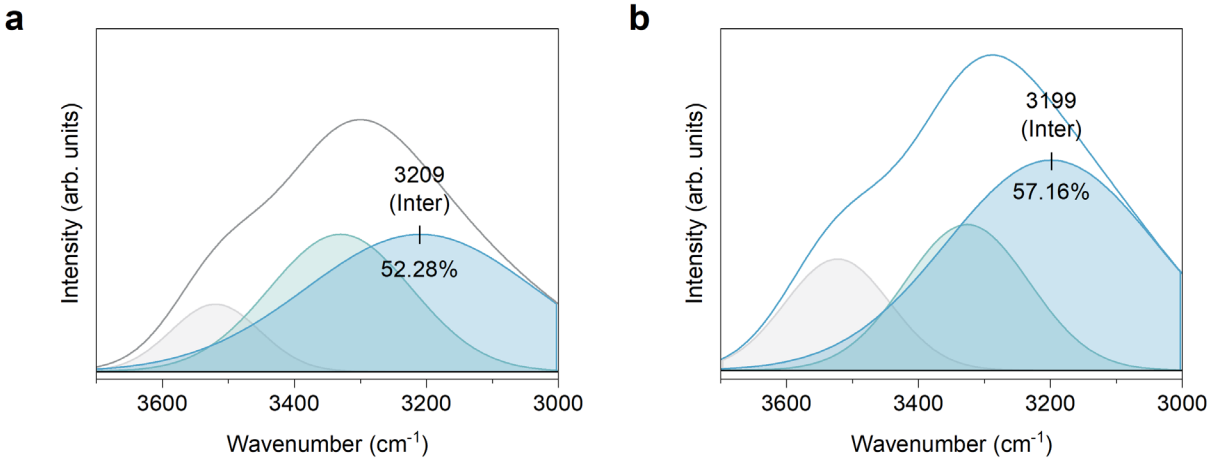

Supplementary Fig. 4. ATR-FTIR spectra of **a,** CNF and **b,** ONF cellulose papers.

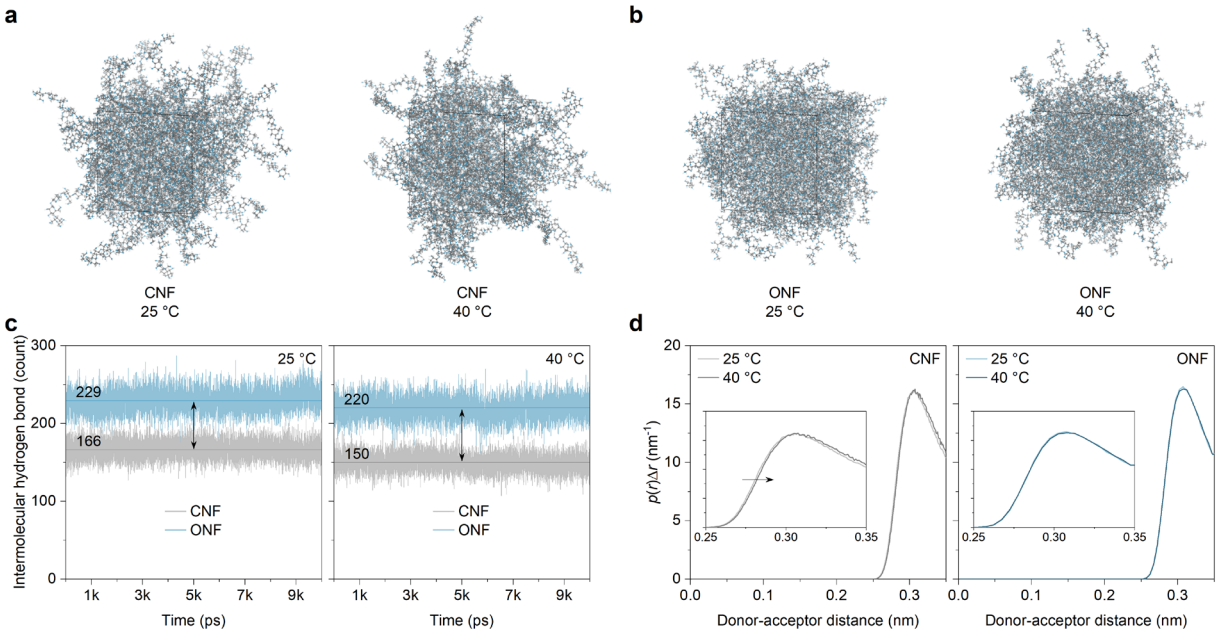

Supplementary Fig. 5. Molecular dynamics simulation of cellulose hydrogen bond energy changes at 25 °C and 40 °C. **a,** CNF cluster model. **b,** ONF cluster model. **c,** Variation in the number of intermolecular hydrogen bonds. **d,** Variation in the length of intermolecular hydrogen bonds. Gray, white, and blue atoms denote C, H, and O, respectively.

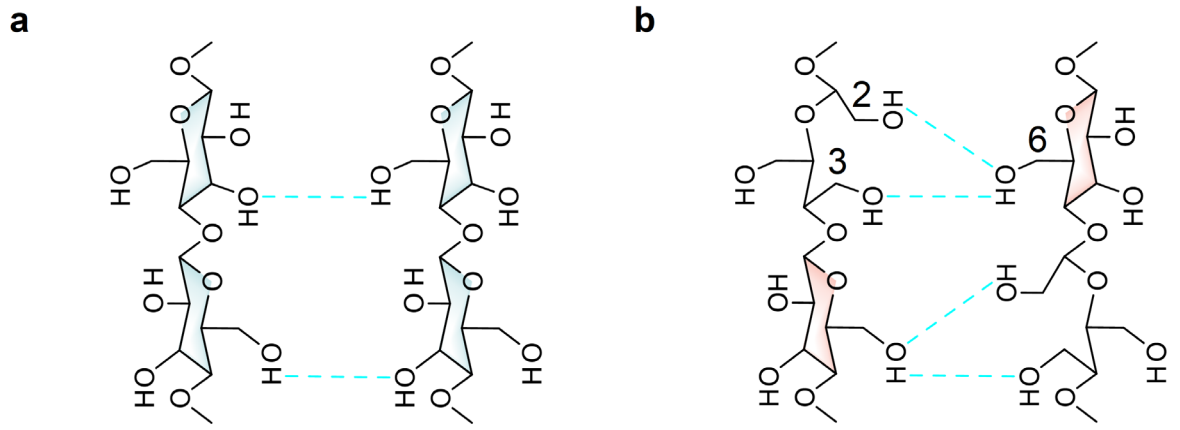

Supplementary Fig. 6. The schematic illustrations of interchain hydrogen bond distributions in **a,** CNF and **b,** ONF (as derived from the isosurface analysis in Fig. 2e).

Supplementary Note 2

A CNF chain composed of 24 anhydroglucose units (AGUs) adopts a loosely packed helical conformation (**Supplementary Fig. 7**)., characterized by an inner diameter (d_1) of ~9.5 Å, an outer diameter (d_2) of ~28.5 Å, and a helical pitch (d_3) of ~12 Å. In this configuration, hydroxyl groups are randomly distributed on both the inner and outer surfaces of the helix, leading to spatially dispersed interaction sites and inefficient cooperative binding toward iodine species. In contrast, ONF—constructed from the same number of AGUs but subjected to targeted ring opening—exhibits a conformationally optimized helical structure. Specifically, ONF shows a significantly reduced inner diameter ($d_1 \approx 4$ Å) and outer diameter ($d_2 \approx 20$ Å), along with an expanded pitch ($d_3 \approx 25.5$ Å). Importantly, the hydroxyl groups in ONF are preferentially oriented toward the outer surface of the helix, rather than being randomly distributed. This conformational reorganization endows ONF with a compact, size-matched nanocavity that accommodates linear I_3^- species (~2.2 Å), while the outward-oriented hydroxyl groups and extended helical pitch create a dense, cooperative hydrogen-bonding network capable of strong I···H-O interactions. Importantly, despite partial hydrogen-bond consumption during polyiodide adsorption, ONF retains a substantially higher fraction of intermolecular hydrogen bonding than CNF, enabling simultaneous iodine immobilization and preservation of structural integrity during prolonged cycling.

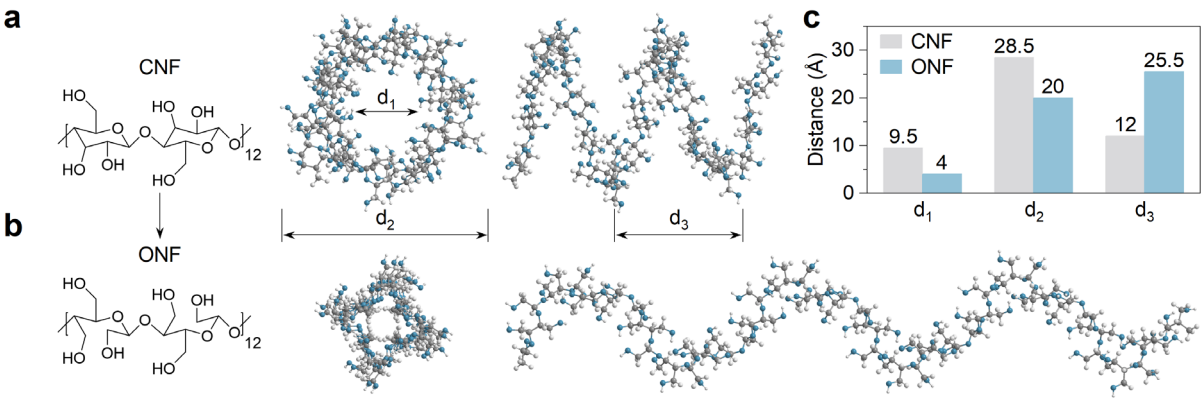

Supplementary Fig. 7. a, CNF and **b,** ONF cellulose conformations with corresponding **c,** structural parameters. Gray, white, and blue atoms denote C, H, and O, respectively.

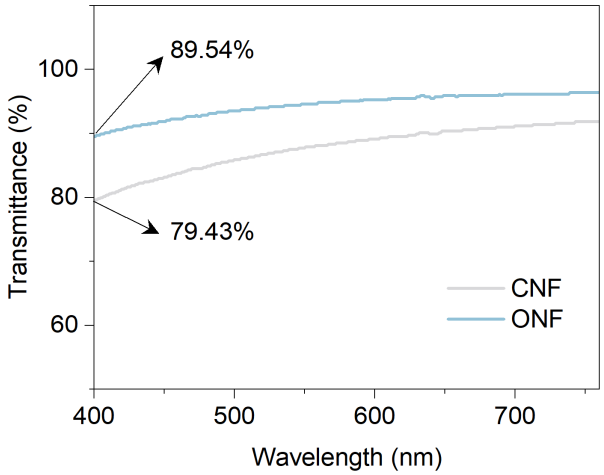

Supplementary Fig. 8. Transmittance spectra of CNF dispersion and ONF dispersion (1.5 mg mL^{-1}, dispersant: deionized water) in the visible wavelength range (400~760 nm).

Supplementary Fig. 9. Optical photographs of CNF dispersion and ONF dispersion after three months of static storage at room temperature.

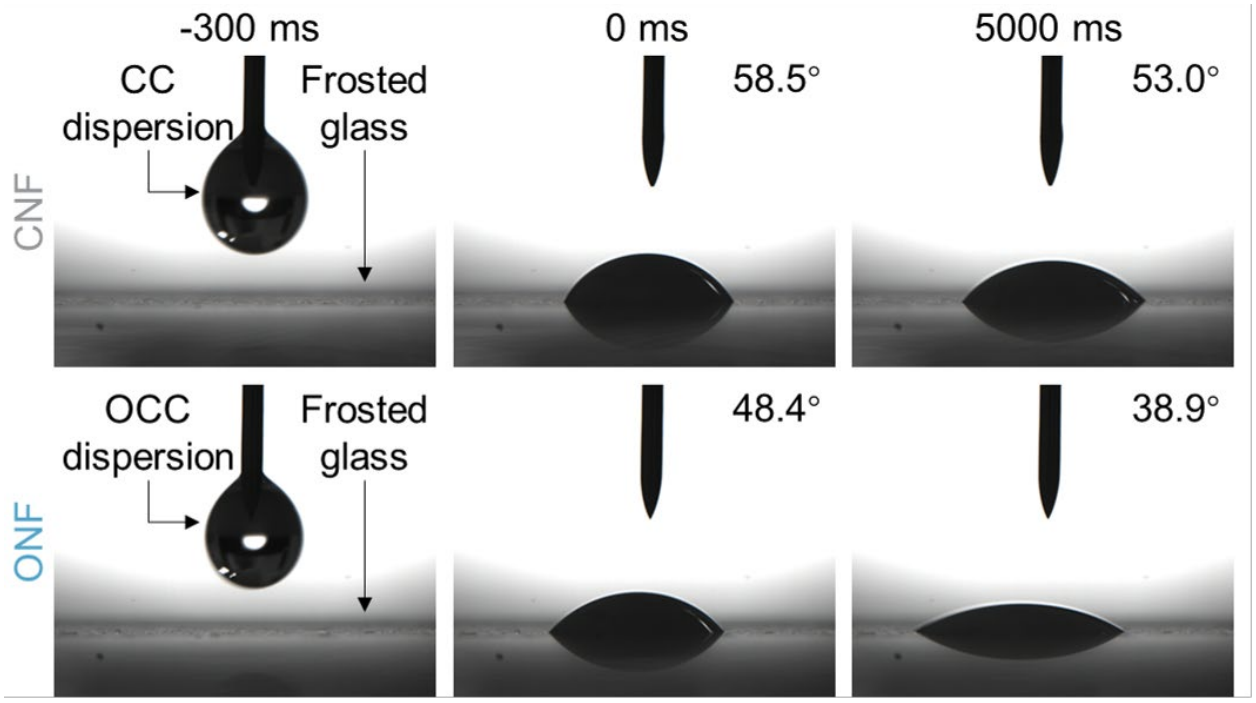

Supplementary Fig. 10. Optical photos of the contact angle test of CNF dispersion and ONF dispersion.

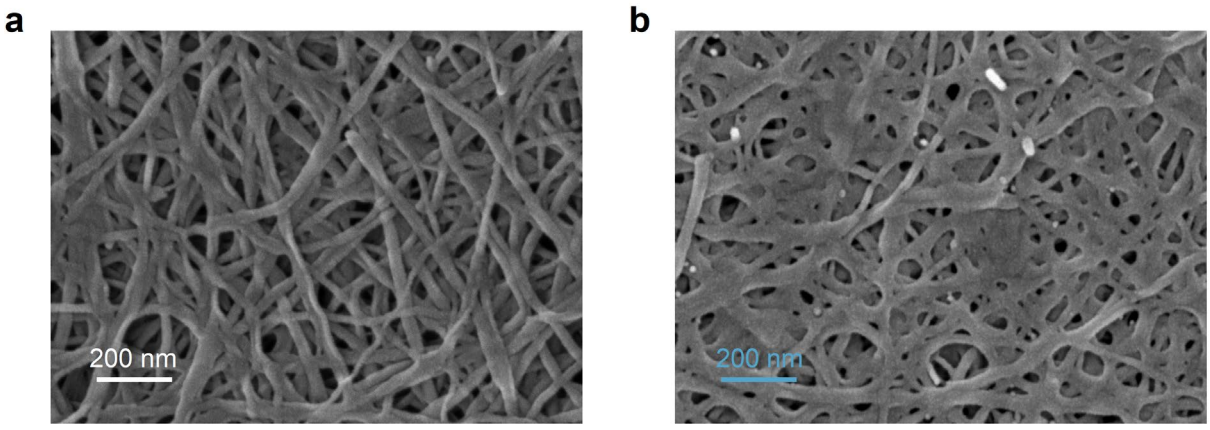

Supplementary Fig. 11. Microstructure of **a,** CNF and **b,** ONF cellulose papers.

Supplementary Fig. 12. Thickness and mass comparison of **a, a1, a2,** CNF and **b, b1, b2,** ONF cellulose papers at equal surface area.

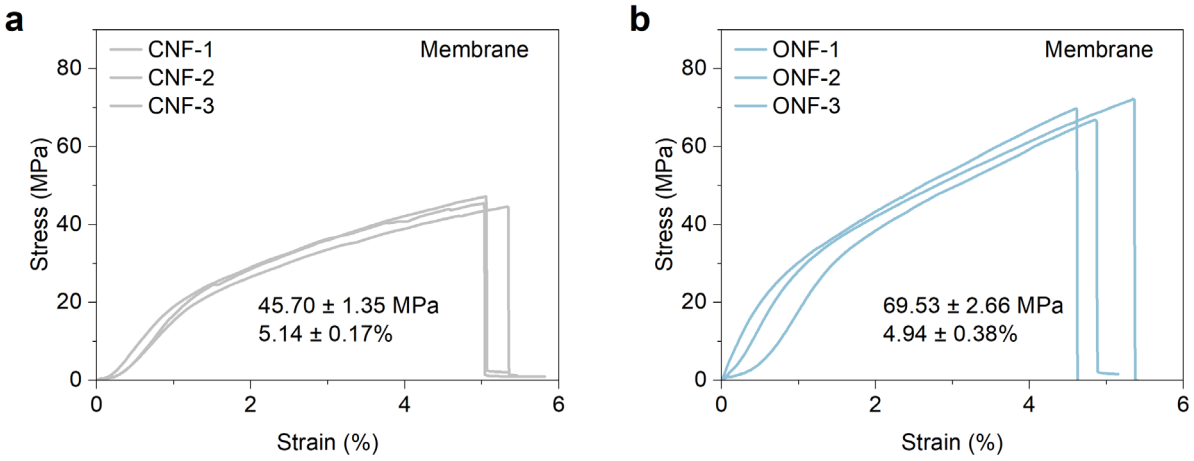

Supplementary Fig. 13. The stress-strain curves of **a,** CNF and **b,** ONF cellulose papers.

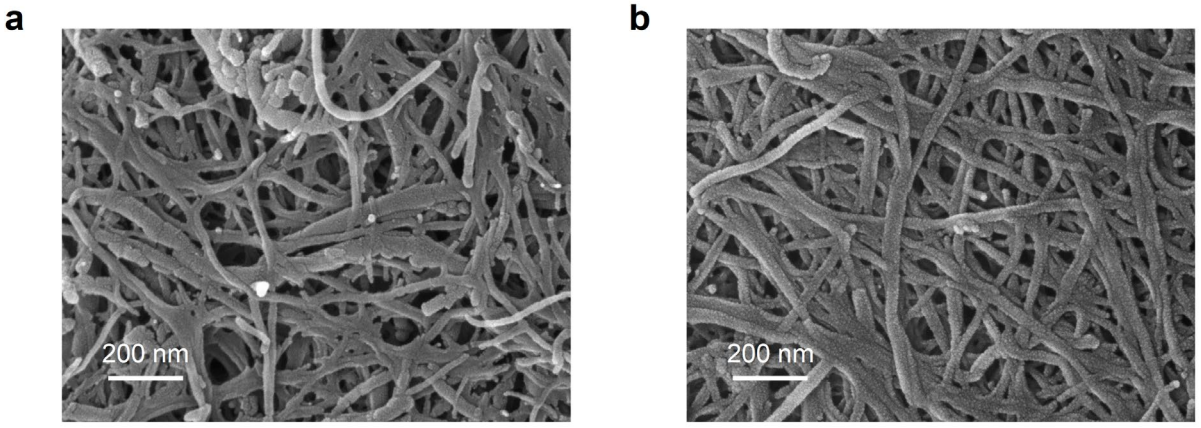

Supplementary Fig. 14. The surface fiber distribution morphology of **a,** CNF- and **b,** ONF-based positive electrodes.

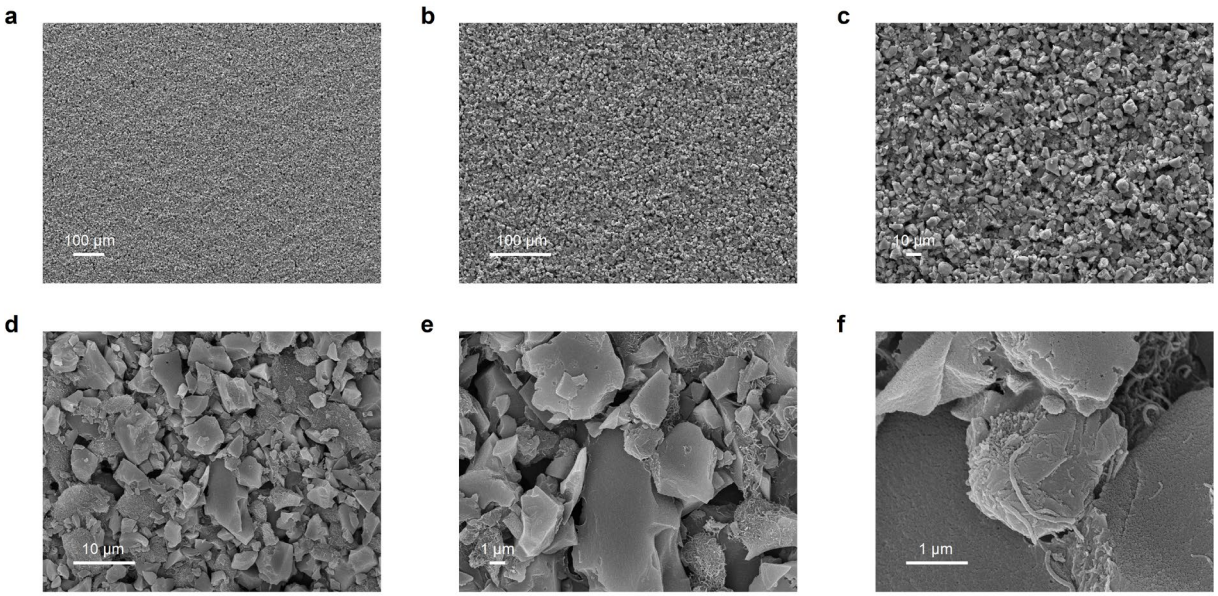

Supplementary Fig. 15. Surface microstructures of PVDF-based positive electrode at different magnifications.

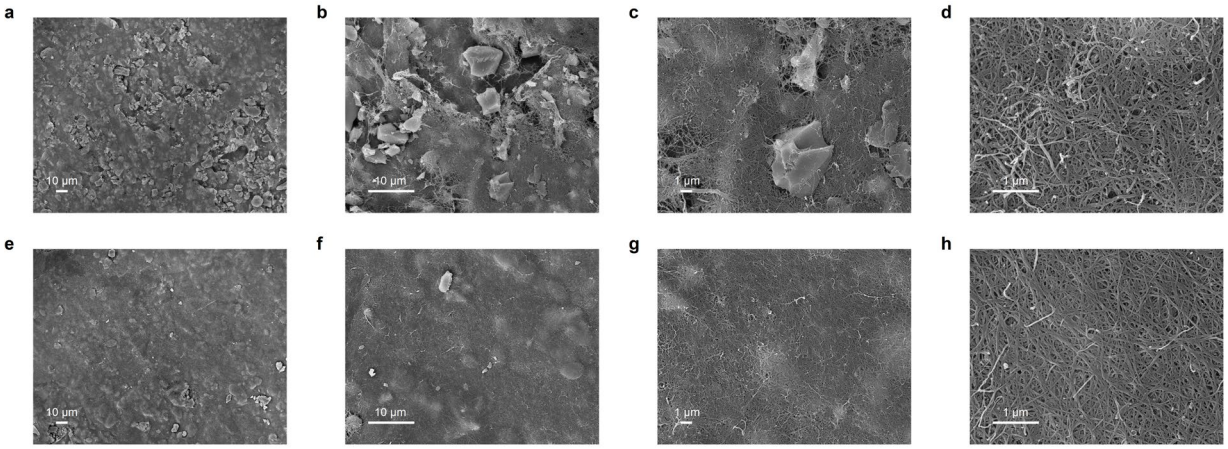

Supplementary Fig. 16. a-d, Surface morphology of the CNF positive electrode at different magnifications. **e-h,** Surface morphology of the ONF positive electrode at different magnifications.

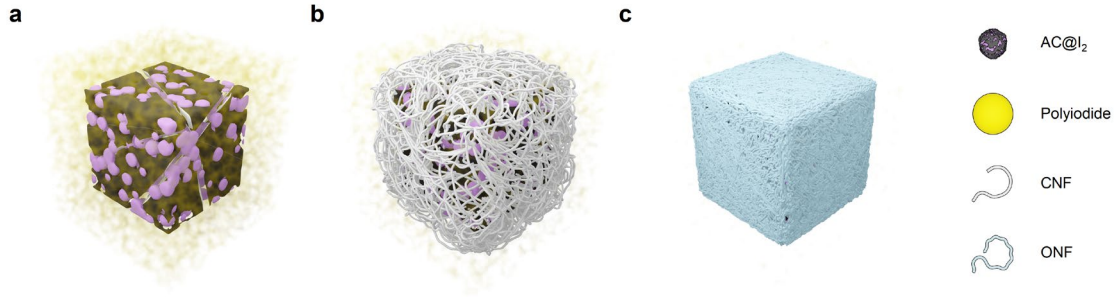

Supplementary Fig. 17. Schematic illustrations of AC@I_2 particle in different iodine positive electrodes: **a,** PVDF, **b,** CNF, and **c,** ONF.

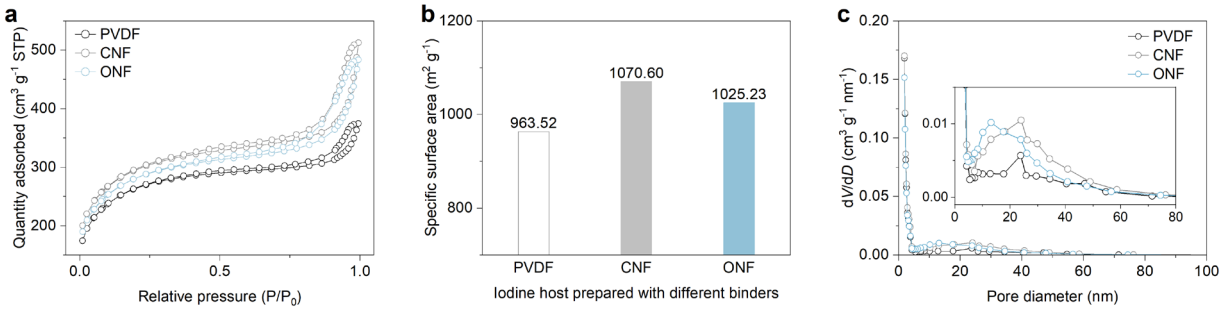

Supplementary Fig. 18. Characterization of porous structures in iodine hosts (without iodine) fabricated using different binders. **a,** Nitrogen adsorption-desorption isotherms. **b,** Specific surface area. **c,** Pore size distribution curves.

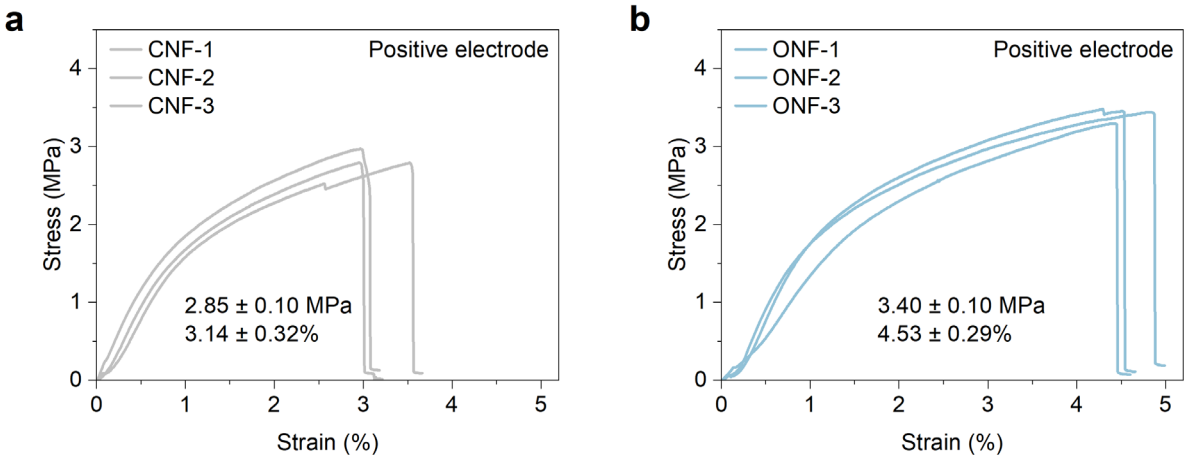

Supplementary Fig. 19. The stress-strain curves of **a,** CNF- and **b,** ONF-based positive electrodes.

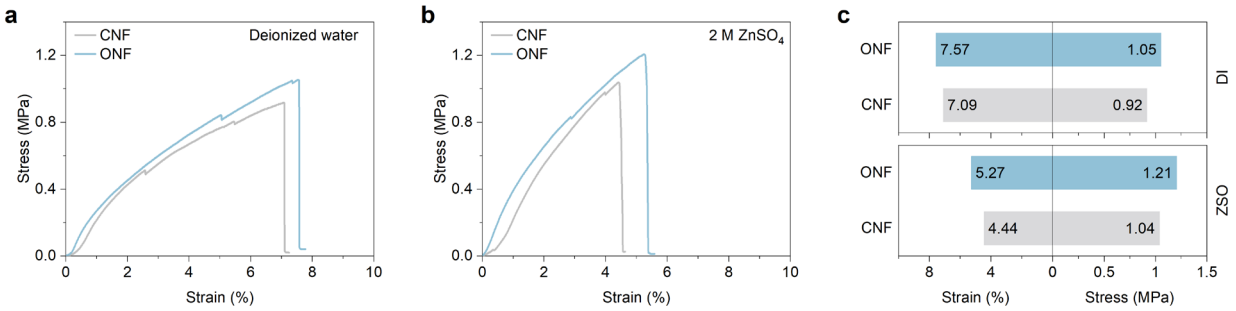

Supplementary Fig. 20. Wet-state mechanical properties of CNF and ONF positive electrodes. **a,** Stress-strain curves of positive electrodes immersed in deionized water. **b,** Stress-strain curves of positive electrodes immersed in 2 M $ZnSO_4$ solution. **c,** Tensile strength and elongation of positive electrodes after immersion in different liquids.

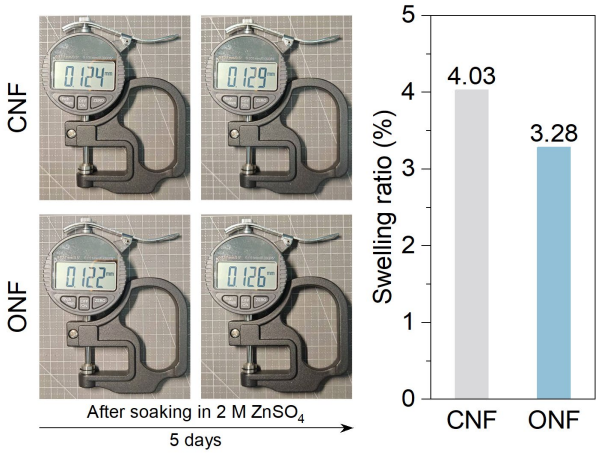

Supplementary Fig. 21. Thickness variation and swelling ratio of CNF and ONF positive electrodes before and after electrolyte immersion.

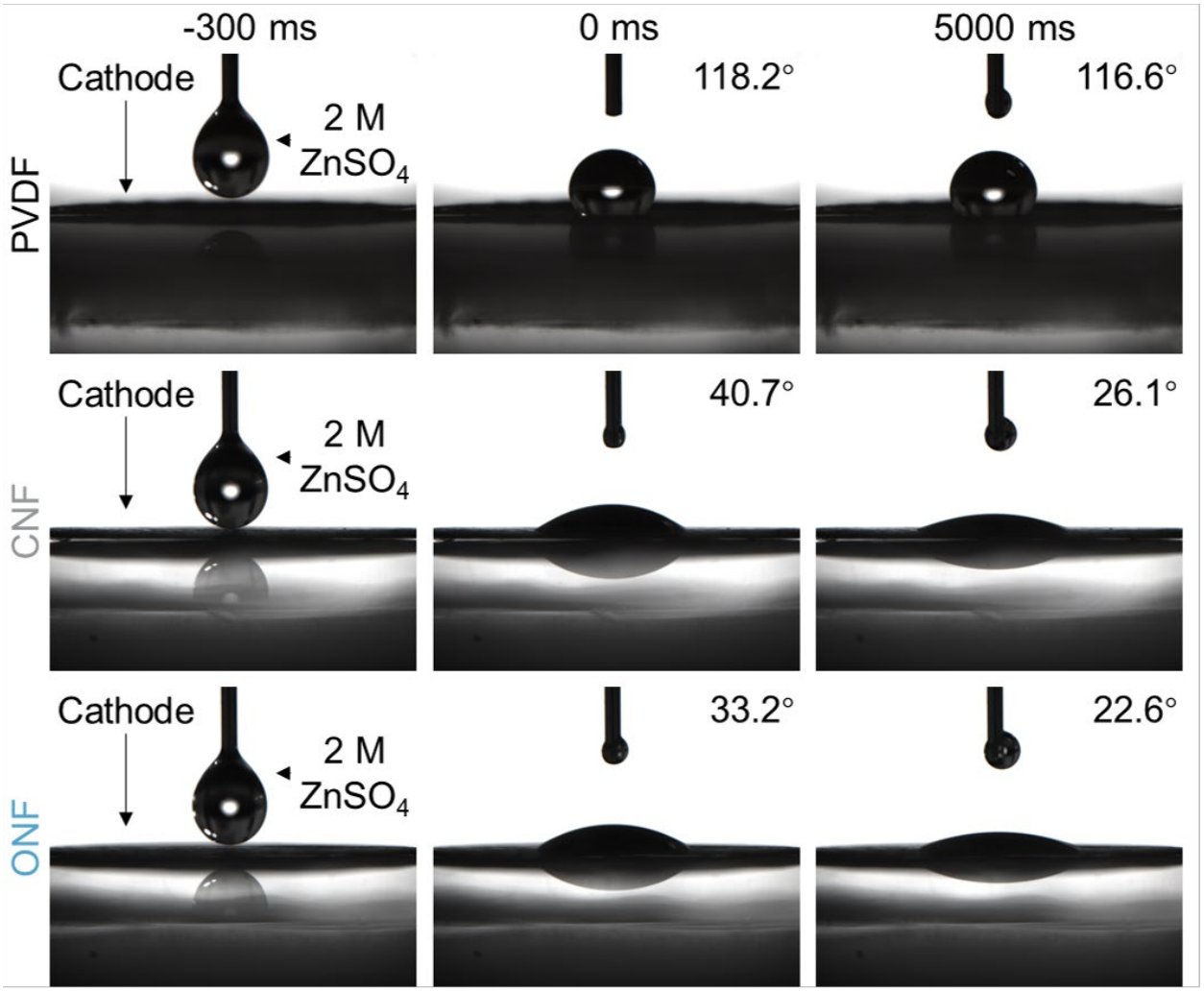

Supplementary Fig. 22. Electrolyte (2 M $ZnSO_4$) wettability of PVDF-, CNF-, and ONF-based positive electrodes.

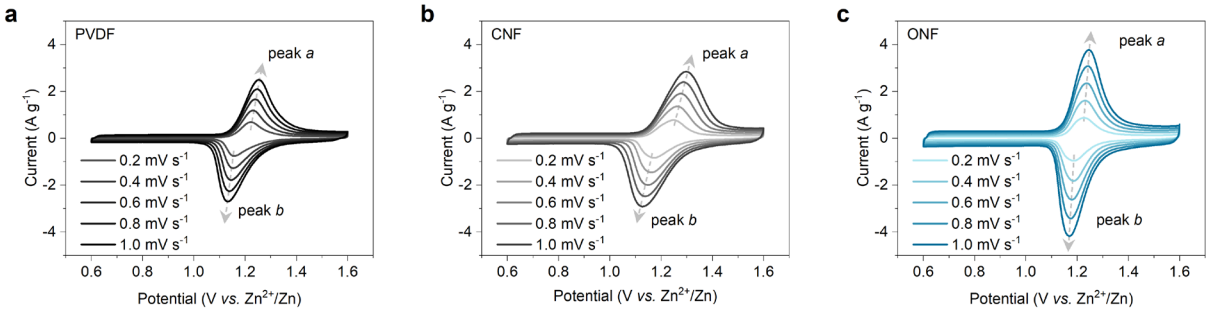

Supplementary Fig. 23. CV profiles of **a,** PVDF-, **b,** CNF-, and **c,** ONF-based positive electrodes at various scan rates. All batteries were tested at 25±1.5 °C.

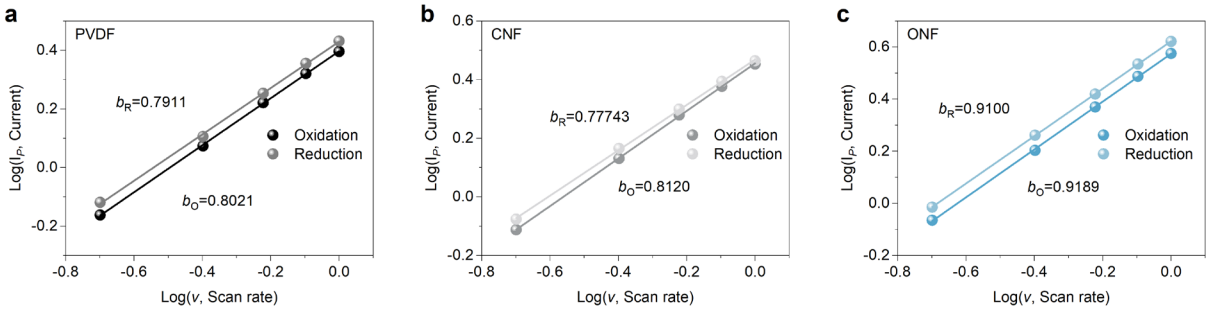

Supplementary Fig. 24. The oxidation peak potential and reduction peak potential as functions of sweep speed for positive electrodes using different binders. **a,** PVDF, **b,** CNF, and **c,** ONF.

Supplementary Note 3

The rising segment (from the equilibrium potential toward the peak potential) of the targeted oxidation/reduction peak in the CV curve is selected, and the corresponding potential-current density data are extracted (**Supplementary Fig. 25**). A linear fit is then performed between the potential and log (current density) to obtain the slope b, which is substituted into the **Equation (4)** to calculate the variation in the reaction energy barrier.

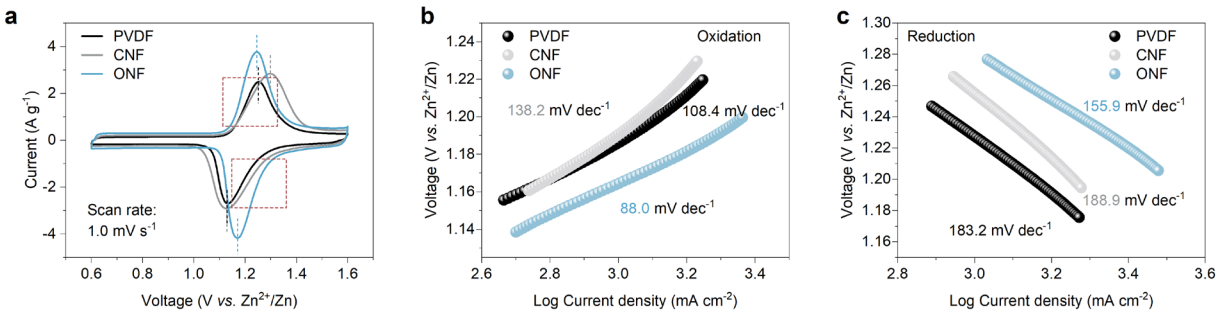

Supplementary Fig. 25. a, CV profiles of PVDF-, CNF-, and ONF-based positive electrodes at 1.0 mV s^{-1}, and comparative analysis of fitted slopes for **b,** oxidation and **c,** reduction peaks. All batteries were tested at 25±1.5 °C.

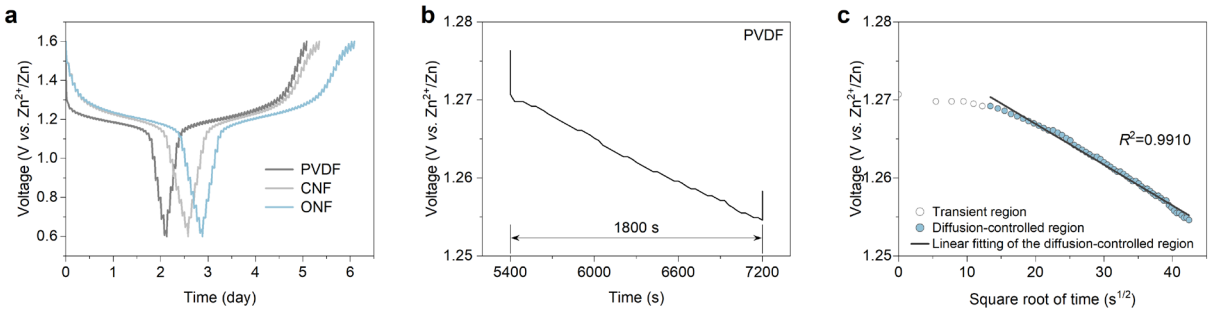

Supplementary Fig. 26. a, GITT profiles of PVDF-, CNF-, and ONF-based positive electrodes. **b,** Transient voltage-time curve during a typical current pulse. **c,** Verification of the linear relationship between cell voltage and the square root of time. All batteries were tested at 25±1.5 °C.

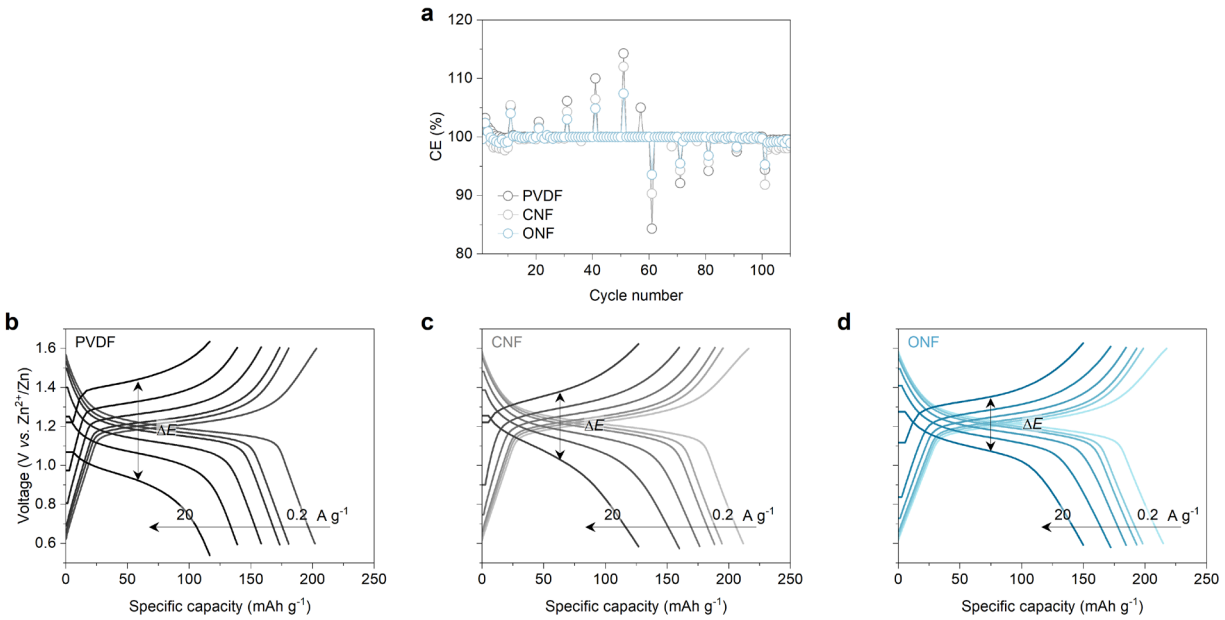

Supplementary Fig. 27. Rate capability of iodine positive electrodes with different binders. **a,** Coulombic efficiency during rate capability tests (with specific currents applied sequentially every 10 cycles: 0.2, 1, 2, 5, 10, 20, 10, 5, 2, 1, 0.2 A g^{-1}). Galvanostatic charge/discharge profiles of **b,** PVDF-, **c,** CNF-, and **d,** ONF-based positive electrodes at varying specific currents (from right to left: 0.2, 1, 2, 5, 10, and 20 A g^{-1}). All batteries were tested at 25±1.5 °C.

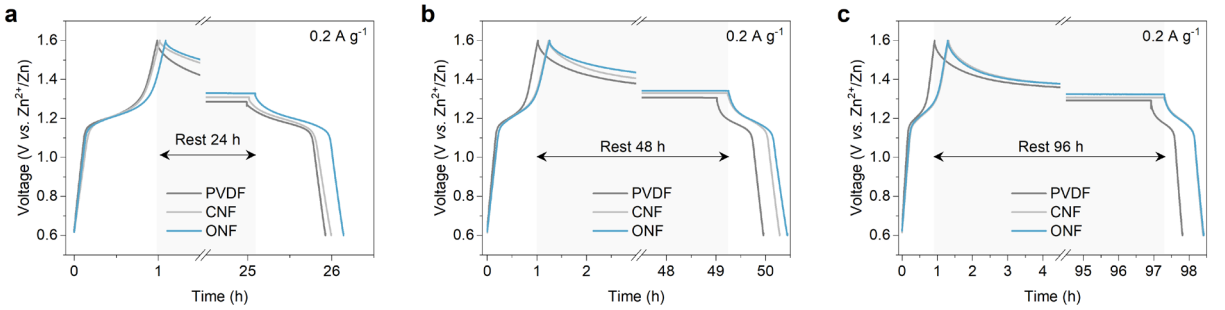

Supplementary Fig. 28. The rest time-voltage curves of Zn||I_2 batteries with different positive electrode binder systems. Rest durations: **a,** 24 h. **b,** 48 h. **c,** 96 h. All batteries were tested at 25±1.5 °C.

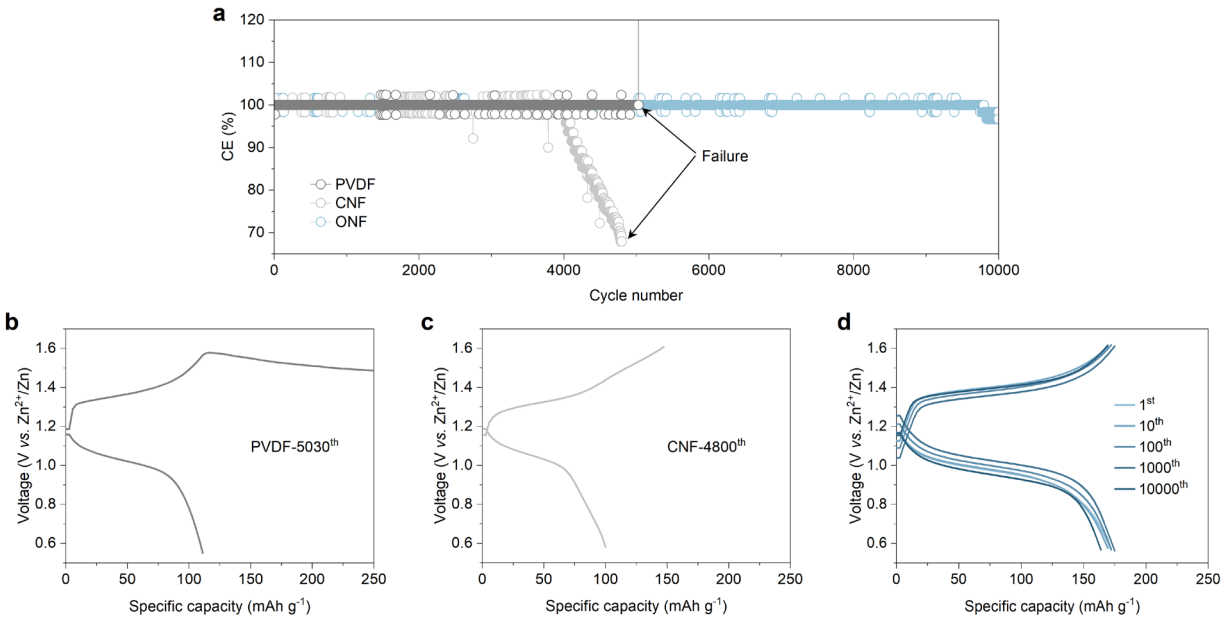

Supplementary Fig. 29. Cycling performance of iodine positive electrodes with different binders. **a,** Coulombic efficiency during cycling performance tests (with a specific current of 10 A g^{-1}). Galvanostatic charge-discharge curves of failed **b,** PVDF-based and **c,** CNF-based positive electrodes. **d,** Galvanostatic charge-discharge curves of the ONF-based positive electrode at different cycle numbers. All batteries were tested at 25±1.5 °C.

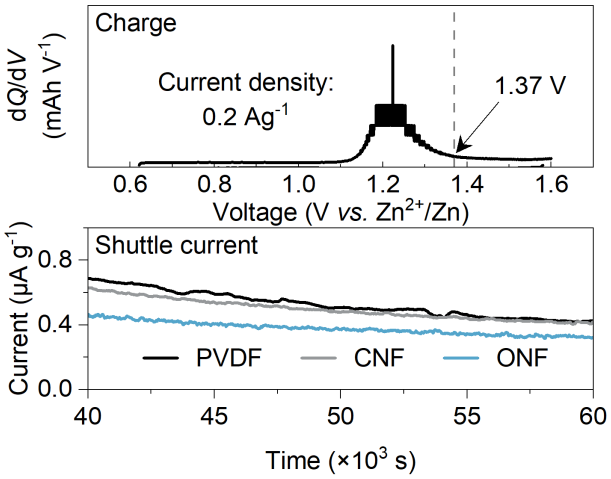

Supplementary Fig. 30. Differential capacity curves (top) of the PVDF-based positive electrode and chronoamperometric profiles (bottom) of different positive electrodes at 1.37 V (vs. Zn^{2+}/Zn). All batteries were tested at 25±1.5 °C.

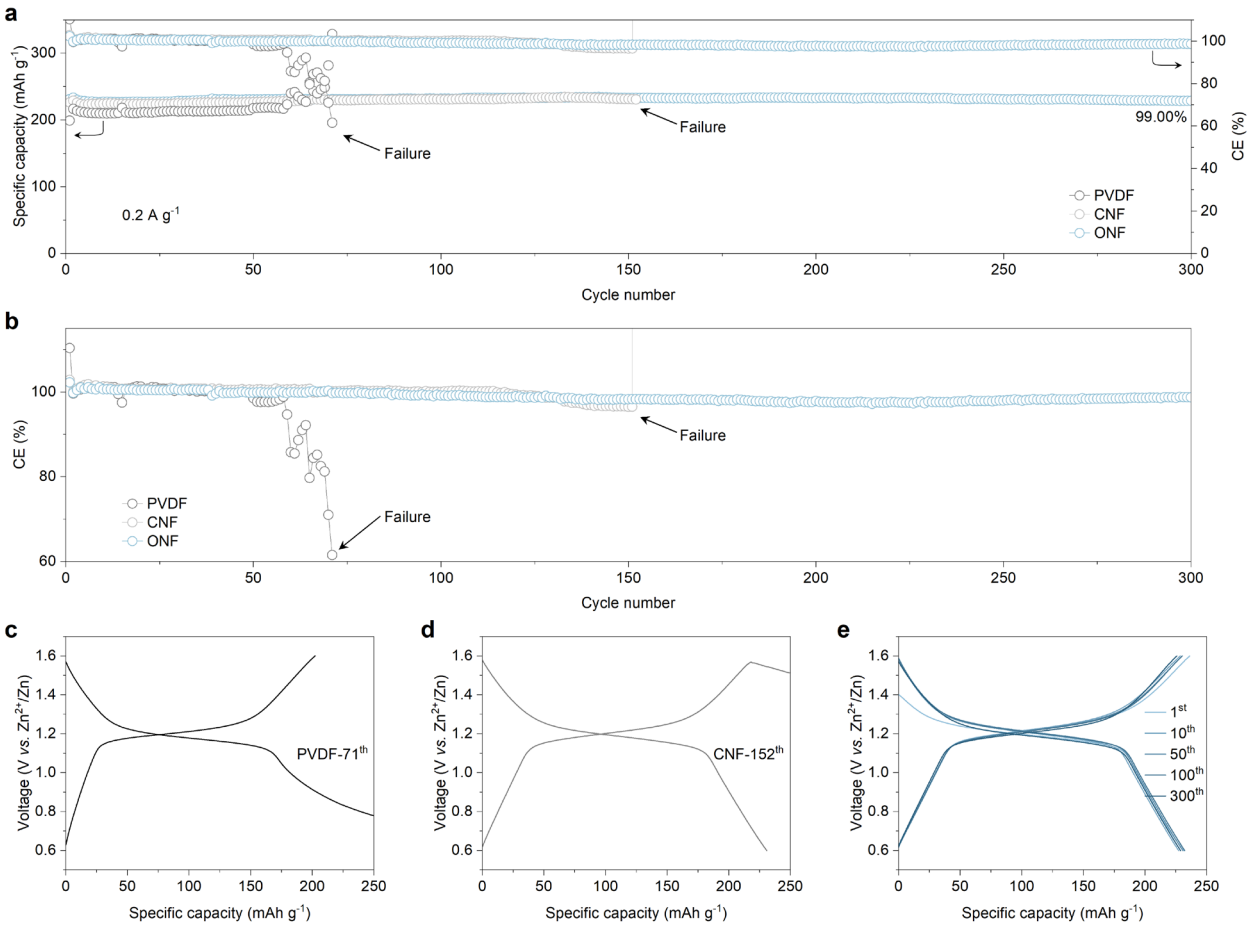

Supplementary Fig. 31. a, Long-term cycling performance of iodine positive electrodes with different binders at 0.2 A g^{-1}. **b,** Coulombic efficiency during cycling performance tests. Galvanostatic charge-discharge curves of failed **c,** PVDF-based and **d,** CNF-based positive electrodes. **e,** Galvanostatic charge-discharge curves of the ONF-based positive electrode at different cycle numbers. All batteries were tested at 25±1.5 °C.

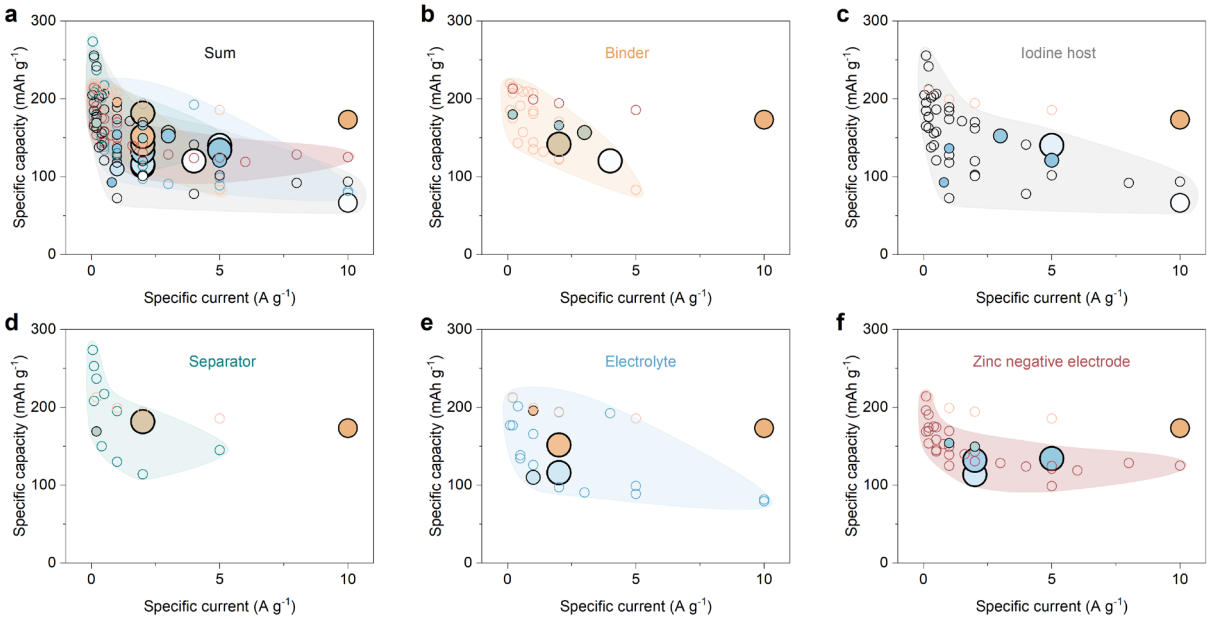

Supplementary Fig. 32. Origin of the color shading in Fig. 4 (hollow circles represent rate performance, solid circles represent cycling performance; the size of the solid circles indicates the number of cycles, and the color represents the remaining specific capacity; see Fig. 4j for details). **a,** Summary of performance comparison among different modification strategies (**b-f**). **b,** Binder. **c,** Iodine host. **d,** Separator. **e,** Electrolyte. **f,** Zinc negative electrode. The source of the literature data shown in this figure can be found in Supplementary Table 4.

Supplementary Note 4

Under high-temperature open-system conditions, polyiodide ions in aqueous solution gradually escape together with water evaporation, leading to a decrease in the residual polyiodide concentration and solution discoloration (**Supplementary Fig. 33**a). The ability of different binders to suppress polyiodide loss can therefore be evaluated by measuring the remaining polyiodide concentration in solution (**Supplementary Fig. 33**b). Because CNF and ONF exhibit different intrinsic background signals in the polyiodide absorption region (**Supplementary Fig. 33**c), background subtraction was performed to obtain the true polyiodide absorbance (**Supplementary Fig. 33**d). The corrected results are summarized in **Fig. 5**a.

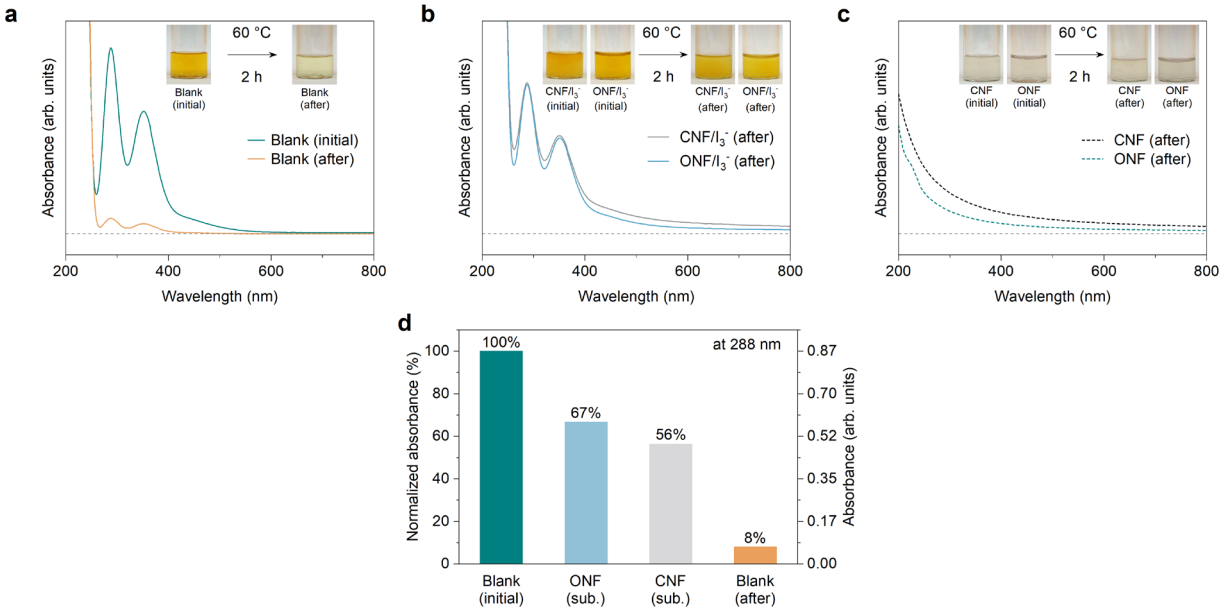

Supplementary Fig. 33. a, UV-Vis spectra of the blank sample before and after heat treatment at 60 °C for 2 h (inset: optical images before and after heating). **b,** UV-Vis absorption spectra of CNF/I_3^- and ONF/I_3^- dispersions after thermal treatment at 60 °C for 2 h (inset: optical images before and after heating). **c,** UV-Vis absorption spectra of CNF and ONF dispersions after thermal treatment at 60 °C for 2 h (inset: optical images before and after heating). **d,** The absorbance of different samples in **Fig. 5a**.

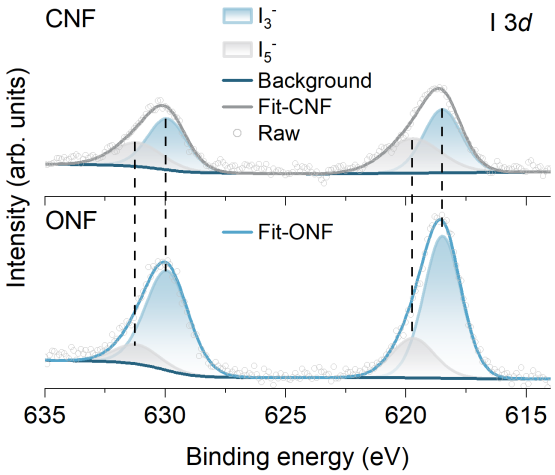

Supplementary Fig. 34. I 3*d* XPS spectra of CNF and ONF cellulose papers after polyiodide adsorption.

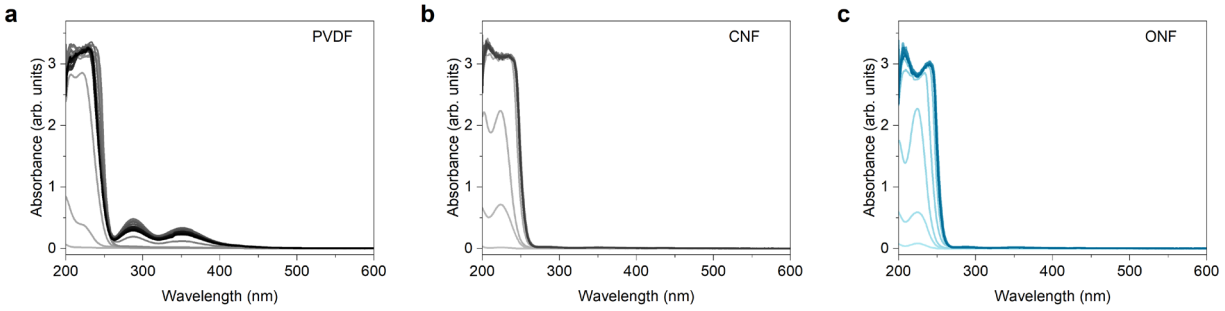

Supplementary Fig. 35. In-situ UV-Vis spectra during charge/discharge processes: **a,** PVDF-, **b,** CNF-, and **c,** ONF-based positive electrodes. The test was conducted at a specific current of 0.1 A g^{-1} and a temperature of 25±1.5 °C.

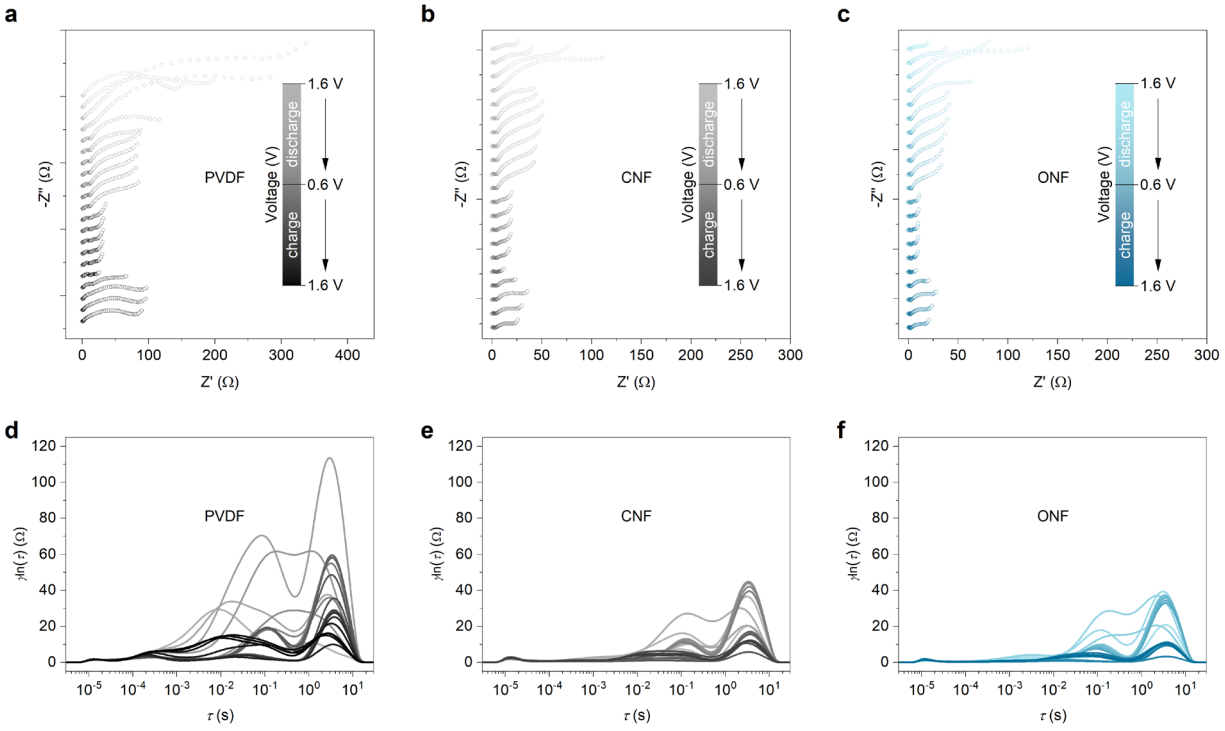

Supplementary Fig. 36. a-c, In-situ EIS and corresponding **d-f,** DRT analysis for **a, d,** PVDF-, **b, e,** CNF-, and **c, f,** ONF-based positive electrodes. The test was conducted at a specific current of 0.2 A g^{-1} and a temperature of 25±1.5 °C.

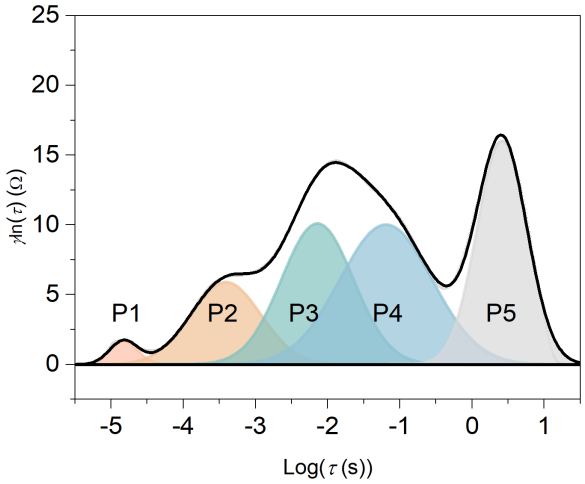

Supplementary Fig. 37. Deconvolution analysis of the DRT for PVDF-based positive electrode at 1.5 V (*vs.* Zn^{2+}/Zn).

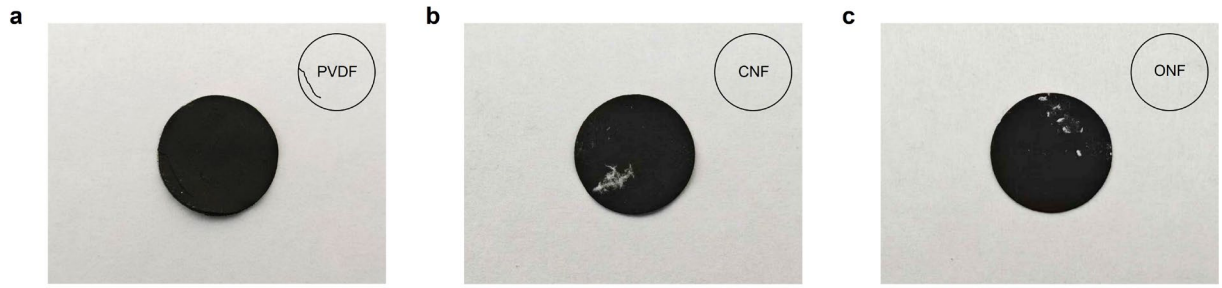

Supplementary Fig. 38. Optical photographs of iodine positive electrodes disassembled after battery cycling. **a,** PVDF-based. **b,** CNF-based. **c,** ONF-based. The battery testing conditions: 10 A g^{-1}, 1000 cycles, 100% SoC (end of test), 25±1.5 °C.

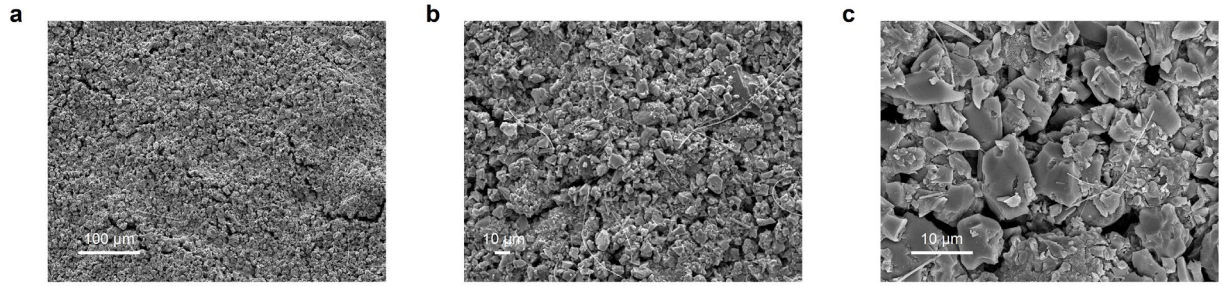

Supplementary Fig. 39. Morphological characterization of the separator-facing surface of cycled PVDF-based positive electrode. Magnifications: **a,** ×200; **b,** ×500; **c,** ×2000. The battery testing conditions: 10 A g^{-1}, 1000 cycles, 100% SoC (end of test), 25±1.5 °C.

Supplementary Note 5

The XRD patterns (**Supplementary Fig. 40**a, b) show that the crystalline structure of both CNF and ONF remained unchanged before and after cycling, indicating that the fundamental cellulose framework was preserved. However, a significant decrease in crystallinity was observed for CNF after cycling. This is further supported by ATR-FTIR results (**Supplementary Fig. 40**c), which show a noticeable reduction in the characteristic absorption peak intensities for hydroxyl (-OH), alkyl (-CH), and glycosidic (C-O-C) bonds in CNF after cycling. This suggests that CNF underwent a certain degree of oxidative degradation and molecular chain scission due to the oxidative action of polyiodides and the mechanical stresses experienced during cycling. In sharp contrast, both the crystallinity and the intensities of the aforementioned characteristic functional group absorption peaks in ONF remained virtually unchanged after cycling (**Supplementary Fig. 40**d). This demonstrates that ONF possesses superior chemical stability against the oxidative environment in zinc-iodine batteries and maintains its structural integrity throughout long-term cycling. This enhanced stability is also the reason why ONF retains a more complete morphology after cycling, as shown in **Fig. 6**c.

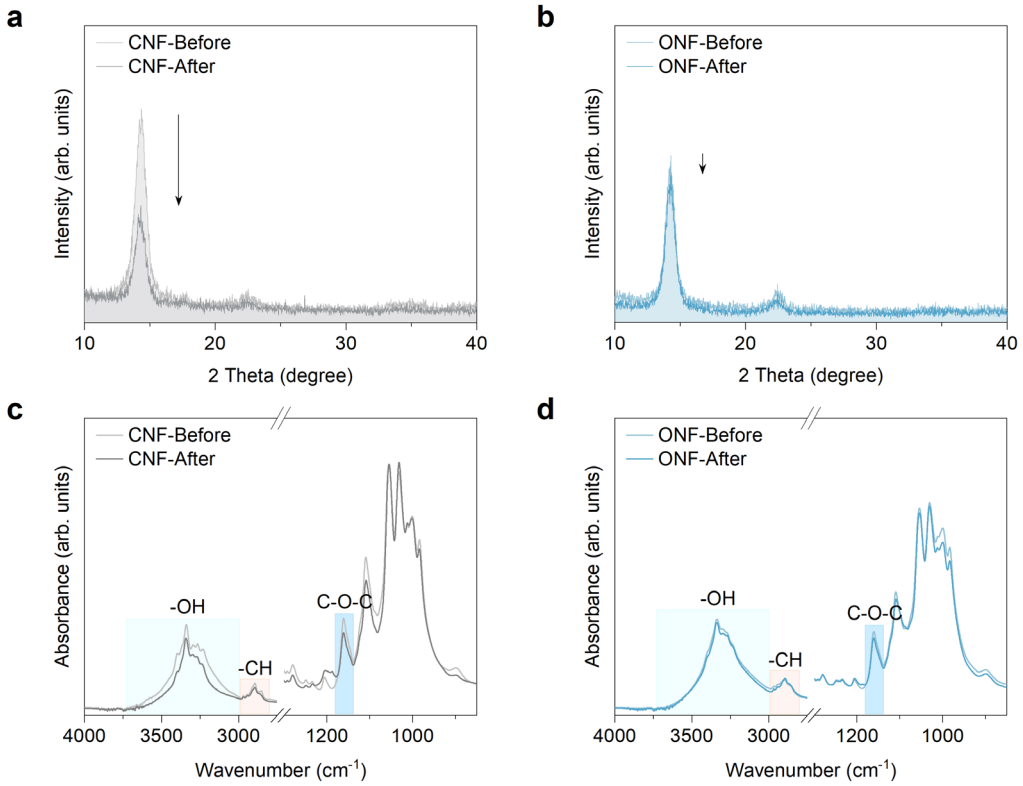

Supplementary Fig. 40. Characterization of Cycling Stability for CNF and ONF. **a, b,** XRD patterns. **c, d,** ATR-FTIR spectra. The battery testing conditions: 10 A g^{-1}, 50 cycles, 100% SoC (end of test), 25±1.5 °C.

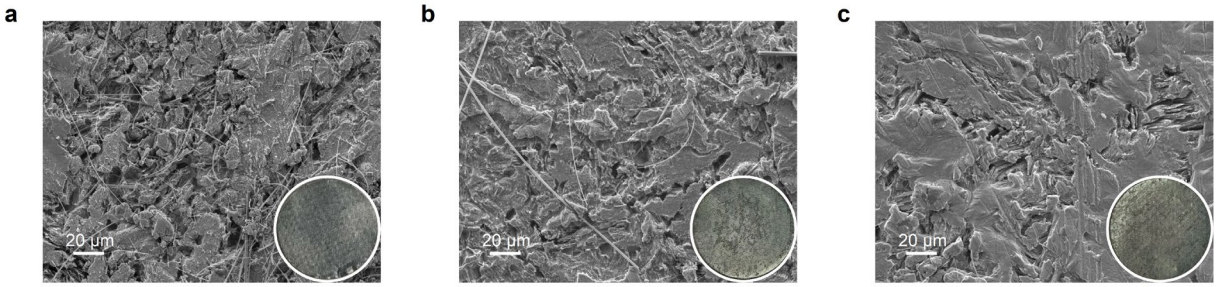

Supplementary Fig. 41. Surface microstructures of cycled zinc negative electrodes on the separator side (insets: optical photographs of zinc negative electrodes): **a,** PVDF, **b,** CNF and **c,** ONF. The battery testing conditions: 10 A g^{-1}, 1000 cycles, 100% SoC (end of test), 25±1.5 °C.

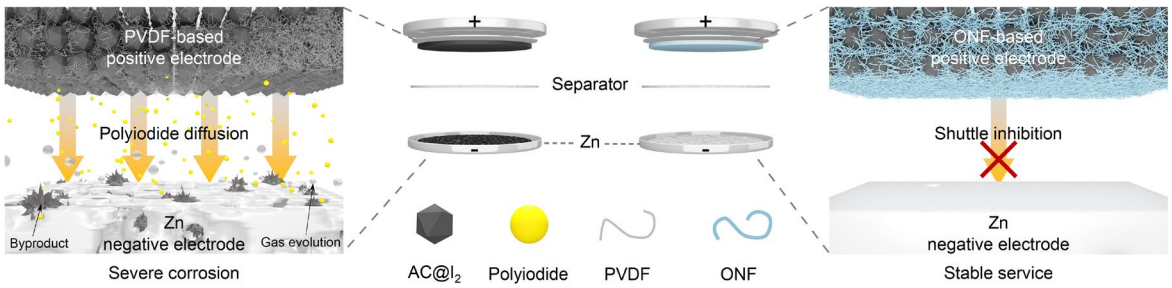

Supplementary Fig. 42. Schematic illustrations of PVDF-based and ONF-based cells.

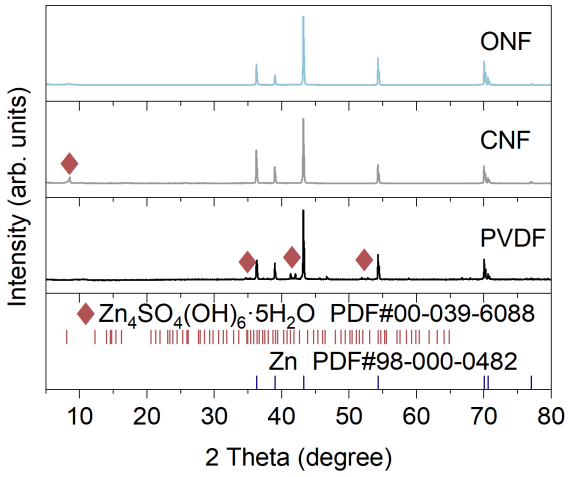

Supplementary Fig. 43. XRD patterns of cycled zinc metal negative electrodes. Testing conditions: 10 A g^{-1}, 1000 cycles, 100% SoC (end of test), 25±1.5 °C.

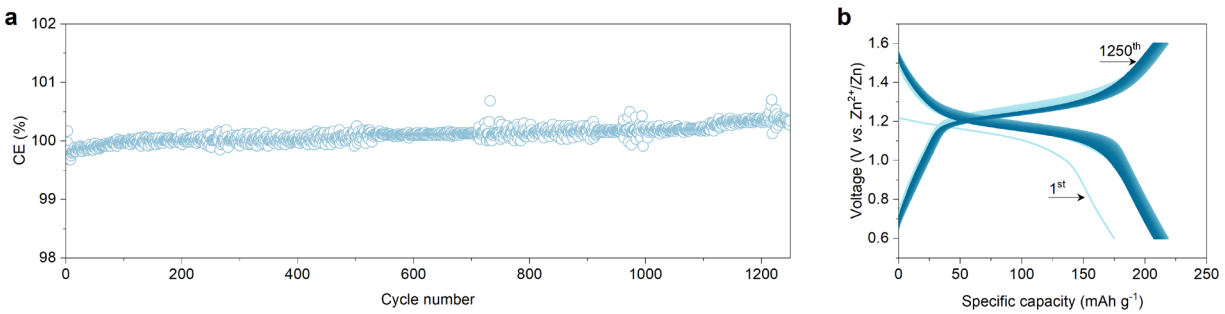

Supplementary Fig. 44. Cycling performance of the pouch cells at 0.2 A g^{-1}. **a,** Coulombic efficiency during cycling performance tests. **b,** Galvanostatic charge/discharge curves. The battery was tested at 25±1.5 °C.

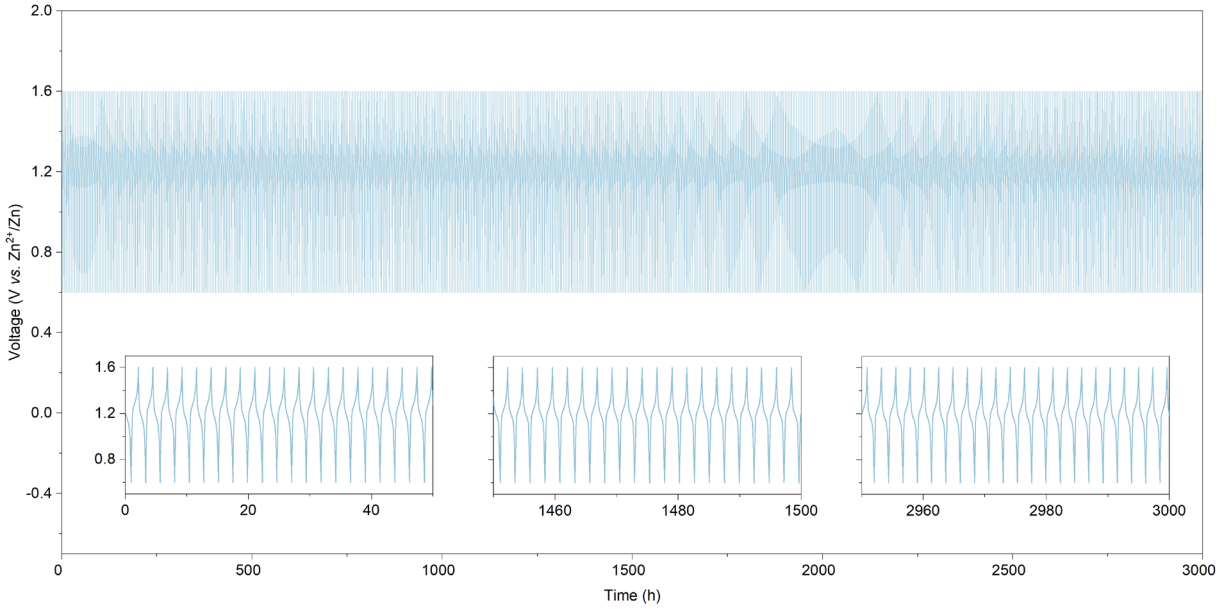

Supplementary Fig. 45. Time-voltage profiles of the pouch cell at 0.2 A g^{-1}. The battery was tested at 25±1.5 °C.

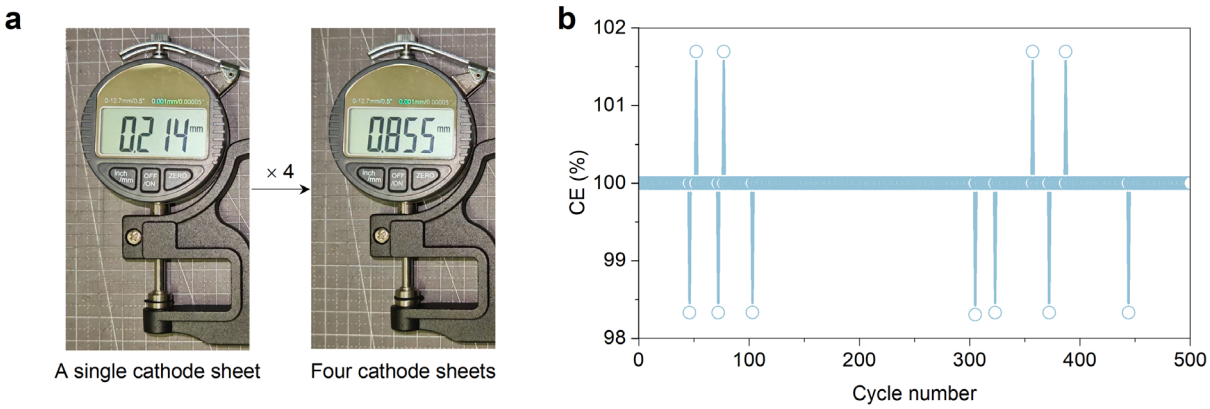

Supplementary Fig. 46. a, The thickness of a single ONF-based positive electrode sheet (left, with an I_2 loading of ~4.0 mg cm^{-2}) and the stacked thickness of four ONF-based positive electrode sheets (right, with an I_2 loading of ~16.0 mg cm^{-2}). **b,** Coulombic efficiency during cycling performance tests of stacked four-layer ONF cathodes at 1 A g^{-1}. The battery was tested at 25±1.5 °C.

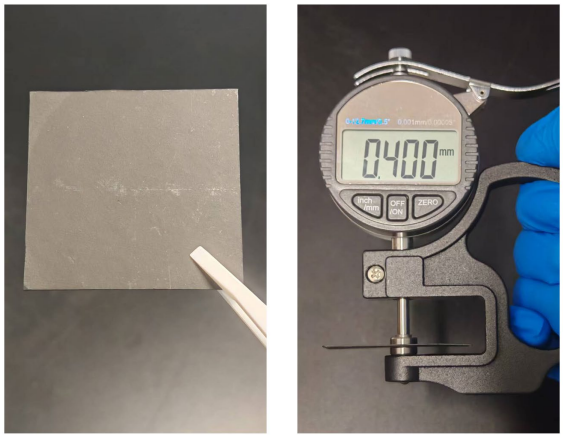

Supplementary Fig. 47. Optical photograph (left) and thickness (right) of ONF-based high-loading iodine positive electrodes prepared by the one-step method.

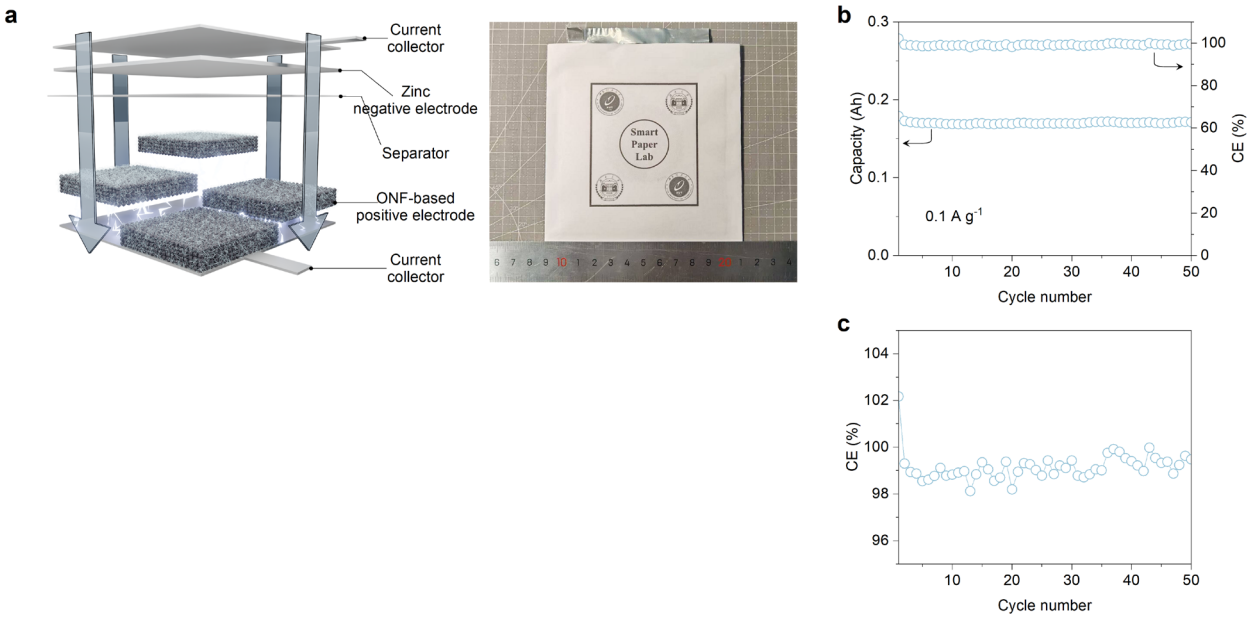

Supplementary Fig. 48. Structural and electrochemical performance of pouch cells with ONF-based high-loading iodine positive electrodes. **a,** Structural schematic (left) and optical photograph (right). **b,** Cycling performance at 0.1 A g^{-1}. **c,** Coulombic efficiency during cycling performance tests. The battery was tested at 25±1.5 °C.

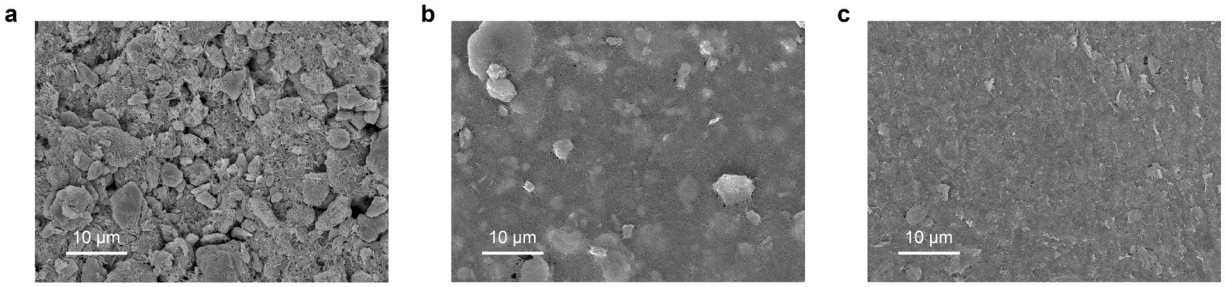

Supplementary Fig. 49. Surface microstructure of V_2O_5 positive electrodes fabricated with different binders: **a,** PVDF, **b,** CNF, and **c,** ONF.

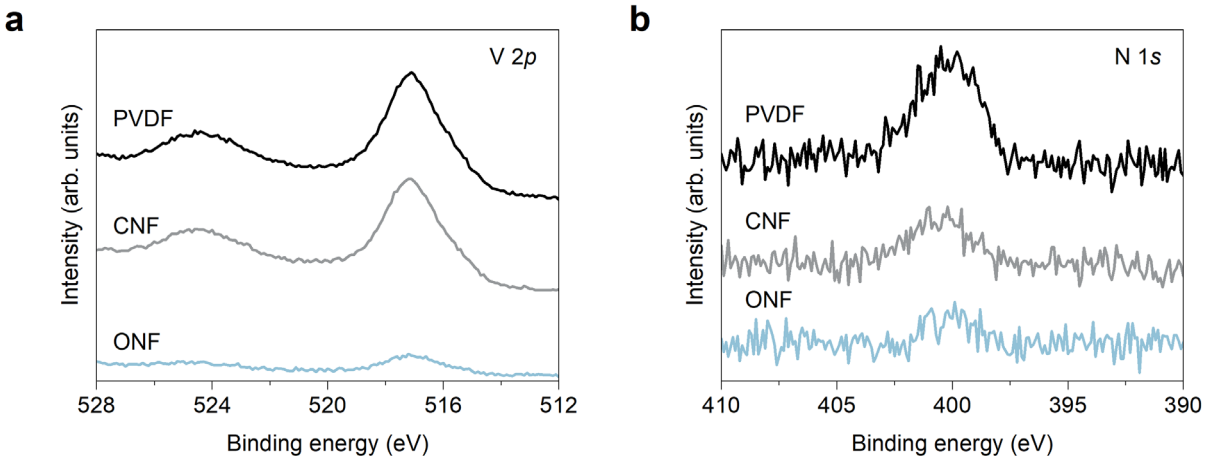

Supplementary Fig. 50. High-resolution XPS spectra of the V_2O_5 positive electrodes: **a,** V 2*p* and **b,** N 1*s*.

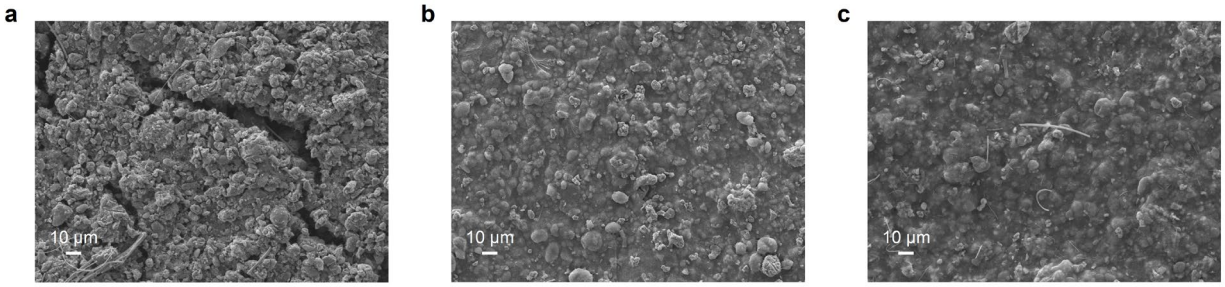

Supplementary Fig. 51. Surface morphologies of cycled V_2O_5 positive electrodes prepared with different binders (separator side, after 5 activation cycles at 0.5 A g^{-1} followed by 50 cycles at 2 A g^{-1}): **a,** PVDF, **b,** CNF, and **c,** ONF.

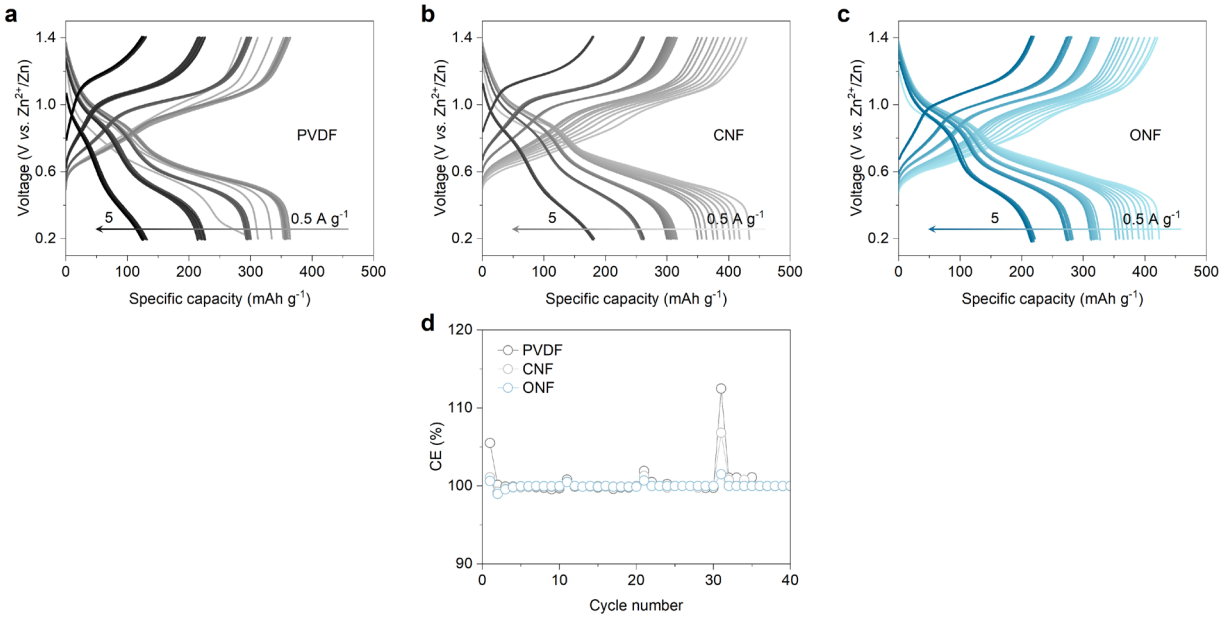

Supplementary Fig. 52. Rate capability of V_2O_5 positive electrodes with different binders. Galvanostatic charge/discharge profiles at various specific currents (from right to left: 0.5, 1, 2, and 5 A g^{-1}): **a,** PVDF, **b,** CNF, and **c,** ONF. **d,** Coulombic efficiency during rate capability tests (with specific currents applied sequentially every 10 cycles: 0.5, 1, 2, 5 A g^{-1}). All batteries were tested at 25±1.5 °C.

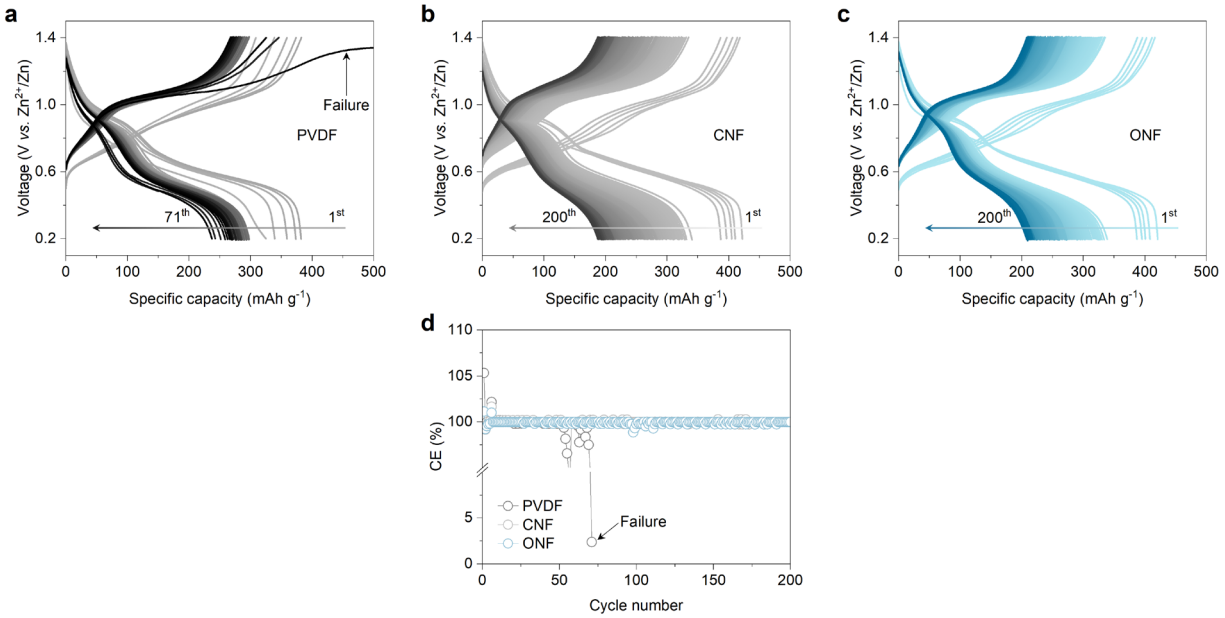

Supplementary Fig. 53. Cycling performance of V_2O_5 positive electrodes with different binders. Galvanostatic charge/discharge profiles (After 5 activation cycles at 0.5 A g^{-1}, cycling was performed at 2 A g^{-1}): **a,** PVDF, **b,** CNF, and **c,** ONF. **d,** Coulombic efficiency during cycling performance tests. All batteries were tested at 25±1.5 °C.

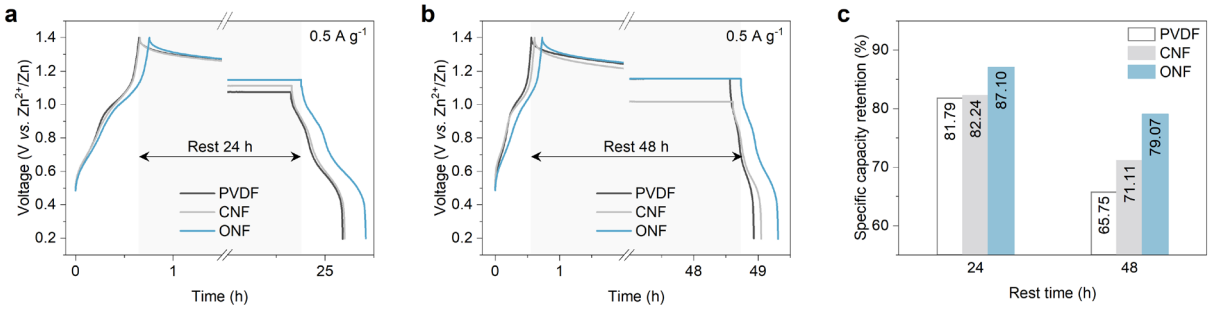

Supplementary Fig. 54. a, Time-voltage curve of Zn||V_2O_5 cell during the 24h resting test. **b,** Time-voltage curve of Zn||V_2O_5 cell during the 48h resting test. **c,** Corresponding capacity retention. All batteries were tested at 25±1.5 °C.

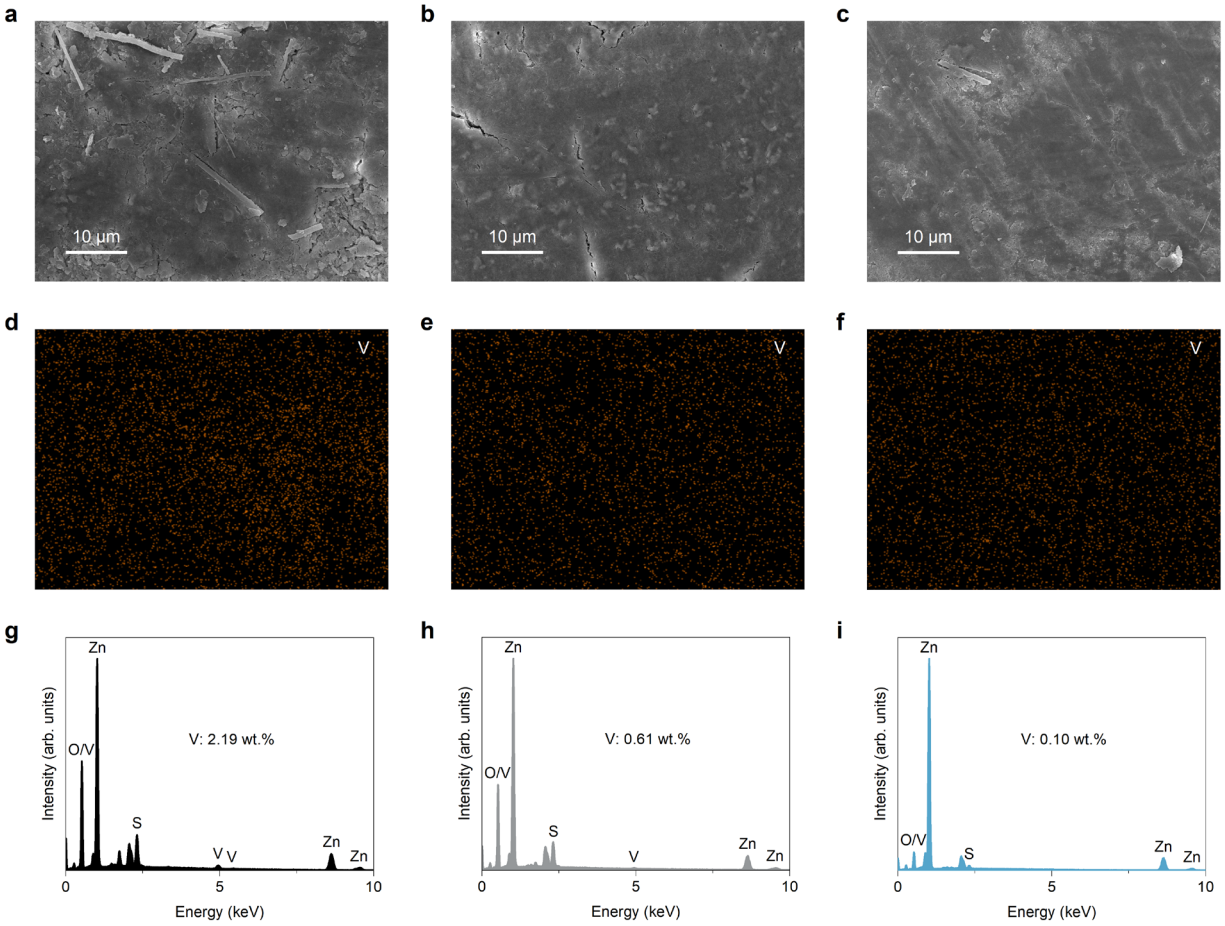

Supplementary Fig. 55. Characterization of cycled zinc metal negative electrodes (separator side, after 5 activation cycles at 0.5 A g^{-1} followed by 50 cycles at 2 A g^{-1}) paired with V_2O_5 positive electrodes prepared with different binders (**Supplementary Fig. 51**): **a-c,** surface morphology, **d-f,** vanadium elemental mapping image, and **g-i,** map sum spectrum for **a, d, g,** PVDF, **b, e, h,** CNF, and **c, f, i,** ONF binder systems. The battery testing conditions: 100% SoC (end of test), 25±1.5 °C.

Supplementary Note 6

Supplementary Fig. 56 presents the surface morphology and corresponding elemental distribution of $LiMn_2O_4$ positive electrodes prepared with PVDF and ONF binders. The PVDF-based positive electrode exhibits a rough surface topography (**Supplementary Fig. 56**a), where $LiMn_2O_4$ particles are directly exposed, as evidenced by the intense Mn signal in the elemental mapping (**Supplementary Fig. 56**b). This morphological characteristic increases the risk of structural degradation for the active material. In contrast, the ONF-based positive electrode demonstrates a uniform surface coverage by ONF fibrous layers (**Supplementary Fig. 56**d), consistent with observations in iodine and V_2O_5 positive electrodes, resulting in significantly attenuated Mn signals (**Supplementary Fig. 56**e). Furthermore, the carbon distribution mapping (**Supplementary Fig. 56**c) reveals poor homogeneity of conductive additives/binders in the PVDF-based positive electrode, which inevitably compromises both electronic conductivity and mechanical integrity. The ONF-modified $LiMn_2O_4$ positive electrode (**Supplementary Fig. 56**f) effectively resolves this issue through optimized component distribution.

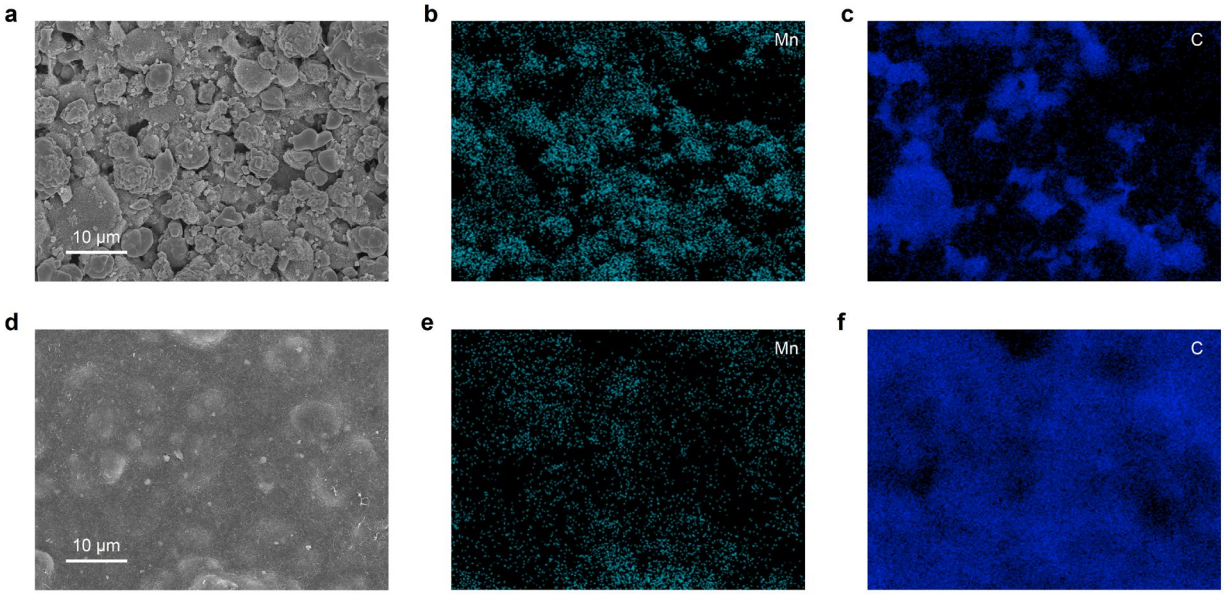

Supplementary Fig. 56. a, d, Surface morphologies and corresponding **b-c, e-f,** elemental distribution images of $LiMn_2O_4$ positive electrodes fabricated with different binders: **a-c,** PVDF, **d-f,** ONF.

Supplementary Note 7

Supplementary Fig. 57 compares the electrochemical performance of $LiMn_2O_4$ positive electrodes fabricated with PVDF and ONF binders. The rate capability tests (**Supplementary Fig. 57**a) demonstrate that the ONF-based positive electrode delivers consistently higher specific discharge capacities across all tested current rates compared to PVDF-based positive electrode. This superiority is further evidenced by galvanostatic charge/discharge profiles, where the ONF-based positive electrode (**Supplementary Fig. 57**c) exhibits significantly better curve overlapping than the PVDF-based positive electrode (**Supplementary Fig. 57**b), indicating enhanced electrochemical stability. The cycling performance tests (**Supplementary Fig. 57**d) reveal more pronounced differences: while the PVDF-based positive electrode (**Supplementary Fig. 57**e) displays capacity fluctuations followed by rapid degradation due to poor structural stability, the ONF-modified positive electrode (**Supplementary Fig. 57**f) maintains exceptional cycling stability throughout the test.

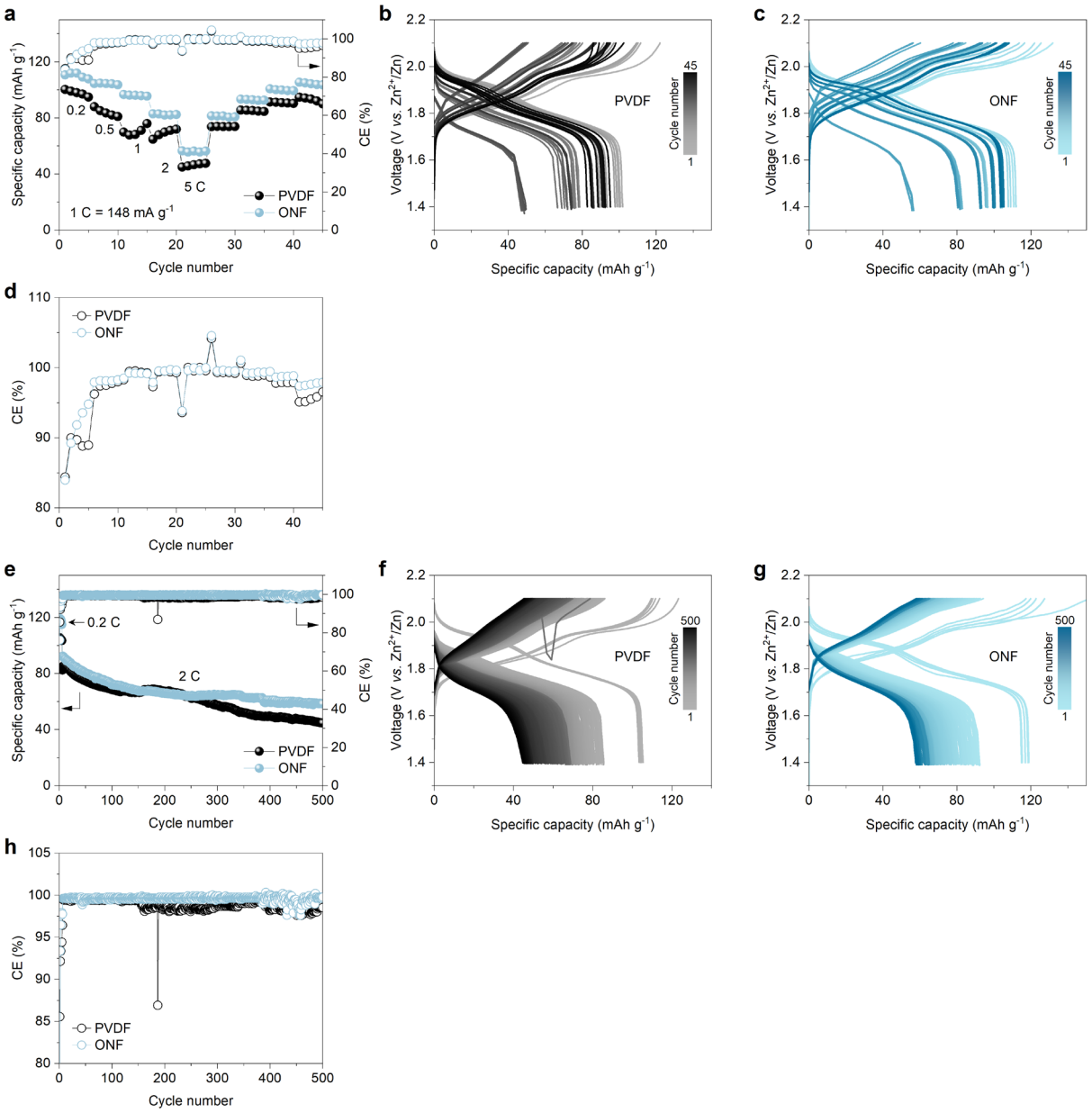

Supplementary Fig. 57. Electrochemical performance of $LiMn_2O_4$ positive electrodes fabricated with different binders. **a,** Rate capability, corresponding **b, c,** galvanostatic charge/discharge profiles, and **d,** Coulombic efficiency during rate capability tests. **e,** Cycling performance, corresponding **f, g,** galvanostatic charge/discharge profiles, and **h,** Coulombic efficiency during cycling performance tests. All batteries were tested at 25±1.5 °C.

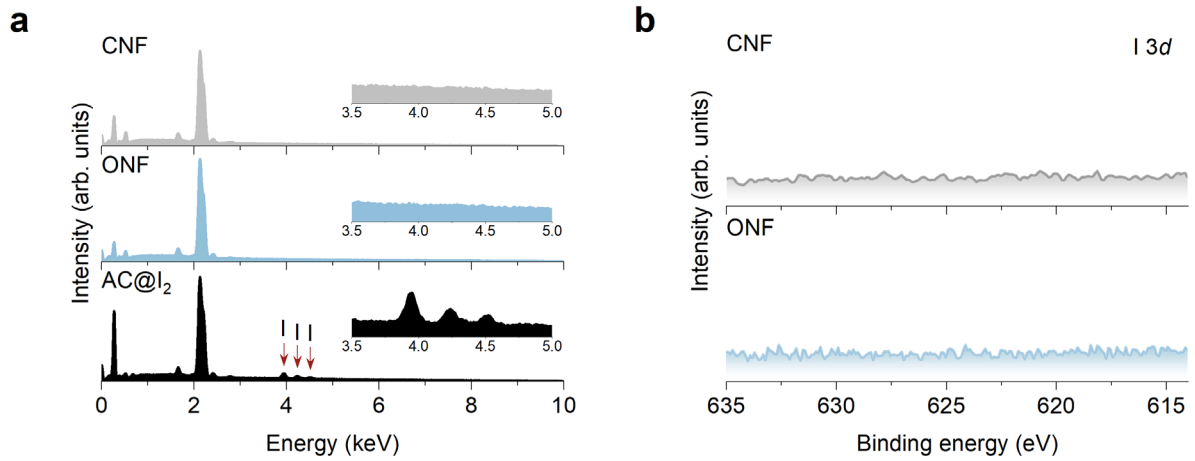

Supplementary Fig. 58. Iodine element detection in fresh cellulose membranes. **a,** EDS spectra of CNF membrane, ONF membrane, and AC@I_2. **b,** XPS I 3*d* spectra of CNF membrane and ONF membrane.

Supplementary Note 8

The ONF binder developed in this work leverages its unique strong hydrogen-bonding network and dense encapsulation capability toward active particles to differentially address the distinct degradation pathways in the two systems (Zn||I_2, Zn||V_2O_5), thereby simultaneously enhancing the discharge specific capacity and cycling stability of both types of batteries while effectively reducing system polarization (**Fig. 4** and **Supplementary Fig. 52, 53**), highlighting its universal applicability.

Specifically, the main failure mechanism of Zn||I_2 battery positive electrode stems from the shuttle effect of polyiodides and the gradual structural loosening of the electrode. The soluble polyiodide ions generated during charge-discharge cycles tend to diffuse into the electrolyte and migrate to the negative electrode, forming a shuttle cycle (**Supplementary Fig. 42**, left) that leads to active material loss and Coulombic efficiency decay. ONF forms a dense coating layer around the iodine host (**Fig. 3**d-f), which not only maintains the structural integrity of the electrode but also serves as a physical barrier to suppress polyiodide dissolution. Meanwhile, the abundant surface hydroxyl groups can chemically adsorb and anchor polyiodides, confining them to the positive electrode side (**Fig. 5**a, b, g). Furthermore, ONF exhibits a certain catalytic effect on the redox reactions of iodine species (**Fig. 4**c, **Fig. 5**h), shortening the lifetime of highly soluble intermediates (**Fig. 5**c-f).

Therefore, ONF can fundamentally suppress the shuttle effect through a "confinement-anchoring-conversion" strategy.

In the case of the Zn||V_2O_5 battery, positive electrode failure primarily originates from the inherent structural instability of V_2O_5, where repeated Zn^{2+} insertion/extraction can lead to crystal-structure collapse accompanied by vanadium dissolution. Dissolved vanadium species can migrate to the Zn negative electrode and damage the negative electrode interface. Here, ONF functions mainly as structural reinforcement and interfacial isolation (**Supplementary Fig. 49-51**). The dense coating layer alleviates volume-expansion stress during cycling and reduces direct contact between V_2O_5 and the electrolyte, thereby suppressing vanadium dissolution. In addition, the hydrogen-bonding network of ONF can partially capture migrating vanadium species, reducing their deposition on the Zn negative electrode. As a result, the vanadium content on the Zn negative electrode decreases to 0.10 wt.% when ONF is used as the binder (**Supplementary Fig. 55**). Consistently, ONF-based Zn||V_2O_5 batteries exhibit improved self-discharge behavior, retaining 87.10% and 79.07% of their initial capacity after 24 h and 48 h of rest, respectively (**Supplementary Fig. 54**).

While the degradation mechanisms of Zn||I_2 and Zn||V_2O_5 systems are fundamentally different, ONF does not rely on a single chemistry-specific reaction. Instead, as a multifunctional binder, ONF provides robust physical confinement, interfacial stabilization, and enhanced charge-transport continuity, which effectively mitigate the dominant degradation pathways in each system.

Supplementary Note 9

Hydroxyl chemistry-driven structural optimization and performance enhancement mechanism

To clarify the intrinsic connection between material design, structural evolution, and electrochemical performance enhancement in this work, this section systematically elaborates the complete structure-property-performance relationship triggered by C2-C3 bond cleavage and governed by hydroxyl chemistry regulation.

Through periodate-borohydride treatment (**Supplementary Fig. 1-2**), selective cleavage of the C2-C3 bonds within anhydroglucose unit (AGU) rings was achieved, yielding oxidized nanofibrillated cellulose (ONF) (**Fig. 2**a-c). This molecular "ring-opening" process disrupts the

intrinsic rigidity of AGU rings and enhances the rotational freedom and accessibility of hydroxyl groups (**Supplementary Fig. 3**), thereby reducing steric constraints on chain packing. Concurrently, charge redistribution induced by bond cleavage drives a moderate contraction of the cellulose helical conformation and promotes the formation of a denser and more stable intermolecular hydrogen-bonding network.

Quantitative Raman analysis (**Supplementary Fig. 4**) confirms a significant increase in intermolecular hydrogen-bond fraction in ONF, while molecular dynamics simulations (**Supplementary Fig. 5**) reveal both an increased hydrogen-bond population and enhanced resistance to thermal perturbation. DFT calculations (**Fig. 2**e and **Supplementary Fig. 6**) further demonstrate that additional energetically favorable hydrogen-bond configurations are accessible between ONF chains. Molecular electrostatic potential analysis (**Fig. 2**f) indicates that hydroxyl hydrogen atoms on the ONF surface exhibit increased positive potential, strengthening their role as hydrogen-bond donors. Together, these molecular- and electronic-level modifications establish the structural foundation for performance enhancement.

These molecular-scale changes directly dictate the macroscopic assembly behavior and interfacial properties of ONF. Enhanced bond rotation and optimized surface potential (**Fig. 2**g) increase chain flexibility and promote outward orientation of active hydroxyl groups (**Fig. 2**d and **Supplementary Fig. 7**). As a result, ONF assembles into densely packed, continuous films during electrode fabrication (**Fig. 3**a and **Supplementary Fig. 12**), forming thin yet compact coating layers on active material particles (**Fig. 3**f and **Supplementary Fig. 16-18**). This architecture imparts superior mechanical robustness in both dry and wet states and significantly suppresses electrode swelling (**Fig. 3**h and **Supplementary Fig. 19-21**), directly reflecting the stability of the underlying hydrogen-bonding network.

During electrochemical operation, this hydrogen-bond-reinforced coating enables multiple synergistic enhancement mechanisms. In Zn||I_2 batteries, it functions as a robust physical barrier that restricts polyiodide dissolution and macroscopic diffusion (**Fig. 5**c-f), while exposed, highly polar hydroxyl groups provide strong chemical anchoring sites. Visual adsorption experiments (**Fig. 5**a), XPS analysis (**Fig. 5**b and **Supplementary Fig. 33, 34**), and DFT adsorption energies (**Fig. 5**g)

collectively confirm the superior polyiodide binding capability of ONF. The synergy between physical confinement and chemical anchoring is essential for suppressing the shuttle effect.

Simultaneously, the dense and integrated coating shortens electron-transport pathways (**Fig. 3**g) while maintaining efficient Zn^{2+} permeability (**Supplementary Fig. 22**), creating an optimized charge-transport microenvironment. This combination lowers iodine redox energy barriers and accelerates reaction kinetics (**Fig. 5**h, i), consistent with reduced polarization, increased pseudocapacitive contribution, and faster kinetics observed experimentally (**Fig. 4**a-c). After prolonged cycling, ONF-based positive electrodes retain structural integrity, whereas CNF-based electrodes exhibit fiber degradation (**Fig. 6**a-c and **Supplementary Fig. 38-40**), directly demonstrating the importance of hydrogen-bond-mediated mechanical stability.

For Zn||V_2O_5 batteries, performance enhancement (**Fig. 6**h, i) likewise originates from the durable ONF coating, which suppresses vanadium dissolution (**Supplementary Fig. 49-51**) and reduces vanadium migration to the Zn negative electrode (**Fig. 6**j and **Supplementary Fig. 55**), demonstrating the universality of this hydrogen-bond engineering strategy.

In summary, precise molecular "surgery" via C2-C3 bond cleavage initiates a cascade of optimizations spanning electronic structure, intermolecular interactions, and macroscopic assembly. The resulting reinforced hydrogen-bond network manifests as a unique coating architecture combining dense packing, high mechanical stability, and high interfacial activity. Through synergistic physical-chemical regulation, this structure enables effective active-species confinement, accelerated redox conversion, optimized charge transport, and long-term electrode stabilization. This explicit structure-property-performance relationship not only explains the superior functionality of ONF as a binder, but also establishes hydroxyl chemistry regulation as a general design principle for next-generation aqueous battery interface materials.

Supplementary Table 1. Synthesis parameters, key properties (yield, extracyclic hydroxyl content), and positive electrode performance (discharge capacity at 20 A g^{-1}) for ONFs prepared from CNF under varying conditions.

Molar ratios ($NaIO_4$/AGU)	Periodate oxidation yield	Borohydride reduction yield	Total yield	Extracyclic hydroxyl content (mmol g^{-1})	Specific capacity at 20 A g^{-1} (mAh g^{-1})
0	-	-	-	-	126.95
0.25	82.54%	98.66%	81.44%	1.7	133.64
1	68.31%	91.94%	62.81%	4	150.01
2	61.50%	68.51%	42.14%	5.1	155.20
4	56.48%	0.46%	0.26%	6.7	-

Supplementary Table 2. Four-probe measurement data for CNF-based and ONF-based electrodes.

Number	Forward voltage (mV)	Reverse voltage (mV)	Electrical resistance (kΩ·cm)	Electrical conductivity (S cm^{-1})
CNF-1	0.03	0.03	0.003	0.3333
CNF-2	0.03	0.03	0.003	0.3333
CNF-3	0.03	0.03	0.003	0.3333
CNF-4	0.04	0.02	0.003	0.3333
CNF-5	0.02	0.04	0.003	0.3333
ONF-1	0.01	0.03	0.002	0.5
ONF-2	0.01	0.02	0.002	0.5
ONF-3	0.01	0.03	0.002	0.5
ONF-4	0.02	0.02	0.002	0.5
ONF-5	0.02	0.02	0.002	0.5

Supplementary Table 3. Range of R_{int}-values and D-values during charge/discharge processes in zinc-iodine batteries with different binder systems.

System	R_{int}-charge (k Ω)	D-charge ($\times10^{-10}$ cm^2 s^{-1})	R_{int}-discharge (k Ω)	D-discharge ($\times10^{-10}$ cm^2 s^{-1})
PVDF-based	0.2909-4.6654	0.6681-2.7518	0.0800-8.8254	2.0262-12.2051
CNF-based	0.1985-2.3474	0.8988-11.1279	0.0993-2.1762	7.6373-14.1112
ONF-based	0.1520-1.8413	1.1320-17.2617	0.0671-1.8058	7.8748-24.3069

Supplementary Table 4. Comparative of electrochemical performance in aqueous Zn||I_2 battery.

Samples		Iodine loading	Rate performance	Cycling stability
Binder	Ref. 1	1-2 mg cm^{-2}	179.8 mAh g^{-1} (0.2697 mAh cm^{-2}) at 0.2 A g^{-1} 123.2 mAh g^{-1} (0.1848 mAh cm^{-2}) at 2 A g^{-1}	142.5 mAh g^{-1} (0.2138 mAh cm^{-2}) at 0.2 A g^{-1} after 1500 cycles
	Ref. 2	2.69 mg cm^{-2}	213.8 mAh g^{-1} (0.5751 mAh cm^{-2}) at 0.2 A g^{-1} 83.0 mAh g^{-1} (0.2233 mAh cm^{-2}) at 5 A g^{-1}	129.4 mAh g^{-1} (0.3750 mAh cm^{-2}) at 2 A g^{-1} after 2700 cycles
	Ref. 3	4.7 mg cm^{-2}	207.2 mAh g^{-1} (0.9738 mAh cm^{-2}) at 0.2 A g^{-1} 156.6 mAh g^{-1} (0.7360 mAh cm^{-2}) at 3 A g^{-1}	151.1 mAh g^{-1} (0.7102 mAh cm^{-2}) at 3 A g^{-1} after 9000 cycles
	Ref. 4	2.3 mg cm^{-2}	219.0 mAh g^{-1} (0.5037 mAh cm^{-2}) at 0.1 A g^{-1} 141.5 mAh g^{-1} (0.3254 mAh cm^{-2}) at 2 A g^{-1}	157.7 mAh g^{-1} (0.3627 mAh cm^{-2}) at 2 A g^{-1} after 48000 cycles
	Ref.5	-	185.5 mAh g^{-1} at 0.1 A g^{-1} 121.8 mAh g^{-1} at 2 A g^{-1}	88.2 mAh g^{-1} at 4 A g^{-1} after 15000 cycles

Iodine host	Ref. 6	3 mg cm^{-2}	176.5 mAh g^{-1} (0.5295 mAh cm^{-2}) at 0.2 A g^{-1} 66.3 mAh g^{-1} (0.1989 mAh cm^{-2}) at 10 A g^{-1}	88.2 mAh g^{-1} (0.0246 mAh cm^{-2}) at 10 A g^{-1} after 10000 cycles
	Ref. 7	1.7 mg cm^{-2}	164.8 mAh g^{-1} (0.2802 mAh cm^{-2}) at 0.1 A g^{-1} 72.3 mAh g^{-1} (0.1229 mAh cm^{-2}) at 1 A g^{-1}	116.6 mAh g^{-1} (0.1982 mAh cm^{-2}) at 0.8 A g^{-1} after 1000 cycles
	Ref. 8	0.8-1.2 mg cm^{-2}	195.1 mAh g^{-1} (0.1951 mAh cm^{-2}) at 0.1 A g^{-1} 93.5 mAh g^{-1} (0.0935 mAh cm^{-2}) at 10 A g^{-1}	113.1 mAh g^{-1} (0.1131 mAh cm^{-2}) at 1 A g^{-1} after 1000 cycles
	Ref. 9	2-2.5 mg cm^{-2}	255.4 mAh g^{-1} (0.5746 mAh cm^{-2}) at 0.1 A g^{-1} 152.3 mAh g^{-1} (0.3427 mAh cm^{-2}) at 3 A g^{-1}	124.0 mAh g^{-1} (0.2790 mAh cm^{-2}) at 3 A g^{-1} after 5900 cycles
	Ref. 10	2 mg cm^{-2}	212 mAh g^{-1} (0.4240 mAh cm^{-2}) at 0.2 A g^{-1} 92 mAh g^{-1} (0.184 mAh cm^{-2}) at 8 A g^{-1}	111.9 mAh g^{-1} (0.2238 mAh cm^{-2}) at 5 A g^{-1} after 5000 cycles
	Ref. 11	0.8-1.2 mg cm^{-2}	241.5 mAh g^{-1} (0.2415 mAh cm^{-2}) at 0.2 A g^{-1} 161.8 mAh g^{-1} (0.1618 mAh cm^{-2}) at 2 A g^{-1}	92.6 mAh g^{-1} (0.0926 mAh cm^{-2}) at 5 A g^{-1} after 20000 cycles
	Ref. 12	3.3 mg cm^{-2}	162.4 mAh g^{-1} (0.5359 mAh cm^{-2}) at 0.2 A g^{-1} 100.8 mAh g^{-1} (0.3326 mAh cm^{-2}) at 2 A g^{-1}	83.6 mAh g^{-1} (0.0119 mAh cm^{-2}) at 2 A g^{-1} after 1000 cycles
Separator	Ref. 13	2 mg cm^{-2}	236.7 mAh g^{-1} (0.4734 mAh cm^{-2}) at 0.2 A g^{-1} 144.9 mAh g^{-1} (0.2898 mAh cm^{-2}) at 5 A g^{-1}	158.3 mAh g^{-1} (0.3166 mAh cm^{-2}) at 2 A g^{-1} after 20000 cycles
	Ref. 14	1.5 mg cm^{-2}	208 mAh g^{-1} (0.3120 mAh cm^{-2}) at 0.1 A g^{-1} 114 mAh g^{-1} (0.1710 mAh cm^{-2}) at 2 A g^{-1}	146.1 mAh g^{-1} (0.2374 mAh cm^{-2}) at 0.2 A g^{-1} after 3600 cycles

Electrolyte	Ref. 15	-	176.8 mAh g^{-1} (0.1 A g^{-1}) 151.6 m mAh g^{-1} (2 A g^{-1})	166.7 mAh g^{-1} at 2 A g^{-1} after 15000 cycles
	Ref. 16	1 mg cm^{-2}	212.3 mAh g^{-1} (0.2123 mAh cm^{-2}) at 0.2 A g^{-1} 192.3 mAh g^{-1} (0.1923 mAh cm^{-2}) at 4 A g^{-1}	185.2 mAh g^{-1} (0.1852 mAh cm^{-2}) at 1 A g^{-1} after 2000 cycles
	Ref. 17	5 mg cm^{-2}	134.4 mAh g^{-1} (0.6720 mAh cm^{-2}) at 0.5 A g^{-1} 79.2 mAh g^{-1} (0.3960 mAh cm^{-2}) at 10 A g^{-1}	99.6 mAh g^{-1} (0.4980 mAh cm^{-2}) at 2 A g^{-1} after 50000 cycles
	Ref. 18	0.8-1.0 mg cm^{-2}	138.4 mAh g^{-1} (0.1246 mAh cm^{-2}) at 0.5 A g^{-1} 81.6 mAh g^{-1} (0.0734 mAh cm^{-2}) at 10 A g^{-1}	98.1 mAh g^{-1} (0.0882 mAh cm^{-2}) at 1 A g^{-1} after 8000 cycles
Zinc negative electrode	Ref. 19	5.4 mg cm^{-2}	168.8 mAh g^{-1} (0.9115 mAh cm^{-2}) at 0.1 A g^{-1} 118.8 mAh g^{-1} (0.6415 mAh cm^{-2}) at 6 A g^{-1}	105.8 mAh g^{-1} (0.5713 mAh cm^{-2}) at 2 A g^{-1} after 65000 cycles
	Ref. 20	6 mg cm^{-2}	214.0 mAh g^{-1} (1.2840 mAh cm^{-2}) at 0.1 A g^{-1} 130.6 mAh g^{-1} (0.7836 mAh cm^{-2}) at 2 A g^{-1}	124.0 mAh g^{-1} (0.7440 mAh cm^{-2}) at 1 A g^{-1} after 2400 cycles
	Ref. 21	1.3 mg cm^{-2}	169.3 mAh g^{-1} (0.2201 mAh cm^{-2}) at 0.2 A g^{-1} 98.8 mAh g^{-1} (0.1284 mAh cm^{-2}) at 5 A g^{-1}	97.0 mAh g^{-1} (0.1261 mAh cm^{-2}) at 2 A g^{-1} after 20000 cycles
	Ref. 22	1-1.5 mg cm^{-2}	174.0 mAh g^{-1} (0.2175 mAh cm^{-2}) at 0.2 A g^{-1} 125.0 mAh g^{-1} (0.1562 mAh cm^{-2}) at 10 A g^{-1}	124.2 mAh g^{-1} (0.1552 mAh cm^{-2}) at 5 A g^{-1} after 60000 cycles
	Ref. 23	-	195.9 mAh g^{-1} (0.1 A g^{-1}) 124.5 mAh g^{-1} (5 A g^{-1})	141.8 mAh g^{-1} at 2 A g^{-1} after 5600 cycles

This work	ONF binder	4 mg cm^{-2}	212.7 mAh g^{-1} (0.8508 mAh cm^{-2}, 2.5611 mWh cm^{-3}) at 0.2 A g^{-1} 173.1 mAh g^{-1} (0.6924 mAh cm^{-2}, 1.9888 mWh cm^{-3}) at 10 A g^{-1} 150.9 mAh g^{-1} (0.6036 mAh cm^{-2}, 1.6121 mWh cm^{-3}) at 20 A g^{-1}	163.9 mAh g^{-1} (0.6556 mAh cm^{-2}, 1.5528 mWh cm^{-3}) at 10A g^{-1} after 10000 cycles

Note: Areal capacity (mAh cm^{-2}) = Specific capacity (mAh g^{-1}) × Iodine loading (g cm^{-2}), Volumetric energy density (mWh cm^{-3}) = (Areal capacity (mAh cm^{-2}) × Average voltage (V)) / Positive electrode thickness (cm).

References

1 Yang, J.-L. *et al.* Janus binder chemistry for synchronous enhancement of iodine species adsorption and redox kinetics toward sustainable aqueous Zn-I_2 batteries. *J. Am. Chem. Soc.* **146**, 6628-6637 (2024).

2 Wang, K. *et al.* An iodine-chemisorption binder for high-loading and shuttle-free Zn-iodine batteries. *Adv. Energy Mater.* **14**, 2304110 (2024).

3 Li, Z. *et al.* Deploying cationic cellulose nanofiber confinement to enable high iodine loadings towards high energy and high-temperature Zn-I_2 battery. *Angew. Chem., Int. Ed.* **63**, e202317652 (2023).

4 Yu, Z.-T. *et al.* Gelatinized starch as a low-cost and bifunctional binder enables shuttle-free aqueous zinc-iodine batteries. *Rare Metals* **43**, 6351-6361 (2024).

5 Liang, X. *et al.* Customized design of R-SO_3H-containing binders for durable iodine-loading cathode of zinc-iodine batteries. *Adv. Energy Mater.* **15**, 2500673 (2025).

6 Zhang, S. J. *et al.* Polyiodide confinement by starch enables shuttle-free Zn-iodine batteries. *Adv. Mater.* **34**, 2201716 (2022).

7 Xu, J. *et al.* ZIF-8 derived porous carbon to mitigate shuttle effect for high performance aqueous zinc-iodine batteries. *J. Colloid Interface Sci.* **610**, 98-105 (2022).

8 Zhu, L. *et al.* Integrated trap-adsorption-catalysis nanoreactor for shuttle-free aqueous zinc-iodide batteries. *Adv. Funct. Mater.* **34**, 2409099 (2024).

9 Qu, W. *et al.* Ni Single-atom bual catalytic electrodes for long life and high energy efficiency zinc-iodine batteries. *Small* **20**, 2310475 (2024).

10 Yang, F. *et al.* Single atom catalysts for triiodide adsorption and fast conversion to boost the performance of aqueous zinc-iodine batteries. *Energy Environ. Sci.* **16**, 4630-4640 (2023).

11 Wei, F. *et al.* Mesoporous poly(3,4-ethylenedioxythiophene): poly(styrenesulfonate) as efficient iodine host for high-performance zinc–iodine batteries. *ACS Nano* **17**, 20643-20653 (2023).

12 Zhao, S. *et al.* Robust I···H-O intramolecular halogen bond boosts reversible I_3^-/I^- redox behavior for sustainable potassium-iodine batteries. *J. Am. Chem. Soc.* **147**, 669-677 (2025).

13 Bi, H. *et al.* Multifunctional janus separator engineering for modulating zinc oriented aspectant growth and iodine conversion kinetics toward advanced zinc-iodine batteries. *Adv. Funct. Mater.* **35**, 2423115 (2025).

14 Yang, P. *et al.* Ionic selective separator design enables long-life zinc-iodine batteries via synergistic anode stabilization and polyiodide shuttle suppression. *Adv. Funct. Mater.* **34**, 2410712 (2024).

15 Wu, H. *et al.* Aqueous zinc-iodine pouch cells with long cycling life and low self-discharge. *J. Am. Chem. Soc.* **146**, 16601-16608 (2024).

16 Hao, J. *et al.* Low-cost and non-flammable eutectic electrolytes for advanced Zn-I_2 batteries. *Angew. Chem., Int. Ed.* **62**, e202310284 (2023).

17 Yang, X. *et al.* Lewis acid-base effect and protonation in electrolyte engineering enable shuttle-free, dendrite-free, and HER-free aqueous Zn-I_2 batteries. *Energy Stor. Mater.* **78**, 104268 (2025).

18 Wang, K. *et al.* A bioimmune mechanism-inspired targeted elimination mechanism on the anode interface for zinc-iodine batteries. *Chem. Sci.* **16**, 7227-7238 (2025).

19 Wen, Z. *et al.* Weakening the space charge layer effect through tethered anion electrolyte and piezoelectric effect toward ultra-stable zinc anode. *Adv. Mater.* **36**, 2407390 (2024).
20 Liu, J., Chen, S., Shang, W., Ma, J. & Zhang, J. In situ formation of 3D ZIF-8/MXene composite coating for high-performance zinc-iodine batteries. *Adv. Funct. Mater.* **35**, 2422081 (2025).
21 Wang, G. *et al.* In situ construction of multifunctional surface coatings on zinc metal for advanced aqueous zinc-iodine batteries. *Adv. Energy Mater.* **14**, 2303221 (2023).
22 Chen, H. *et al.* Bio-inspired biomass hydrogel interface with ion-selective responsive sieving mechanism for corrosion-resistant and dendrite-free zinc-iodine batteries. *Energy Stor. Mater.* **76**, 104113 (2025).
23 Shang, W. *et al.* Boosting Zn||I_2 battery's performance by coating a zeolite-based cation-exchange protecting layer. *Nano-Micro Lett.* **14**, 82 (2022).